LUND UNIVERSITY
Faculty of Science

2D & 3D phase retrieval for propagation-based X-ray phase-contrast tomography

Philip Stjärneblad

Thesis submitted for the degree of Master of Science
Project duration: 8 months

Abstract

Propagation-based X-ray phase-contrast tomography is a 3d imaging technique that utilizes two-dimensional projections from different angular views $\theta = [0, \pi]$ to reconstruct the 3D object information. The phase-contrast allows for higher feature contrast than conventional transmission tomography, as the phase interference gives rise to a sharp edge contrast. These phase fringes can then be utilized in so-called phase retrieval algorithms to retrieve the original imaged object. One of the most commonly used phase retrievals is derived using the transport-of-intensity TIE framework. This method has for a long time been applied in the projections space with single parameters assuming a single material sample. However, recent results indicate that phase retrieval in the reconstructed volume, using 3D TIE phase retrieval, could allow for the use of localized phase information in the retrieval step. This thesis aims to test the underlying approximation that allows for the use of 3D phase retrieval. It will also compare the two methods in unfavourable conditions. Utilizing simulations, we show that the approximation holds for organic materials, re-enforcing the current consensus. Additionally, both the 2d and 3d phase retrieval methods show comparable results in simulations, while laboratory measurement data show the same retrieved structure but with lower contrast.

Contents

List of Abbreviations

PB-PCI Propagation-Based X-ray Phase-Contrast Imaging

PB-PCT Propagation-Based X-ray Phase-Contrast Tomography

FoV Field of View

1   Introduction

X-rays are part of the electromagnetic spectrum and occupy the regions between $0.1 \to 100$ keV, making the radiation highly susceptible for interactions with inner shell electrons. This high chance of interaction makes X-rays ideal for differentiating dense materials, as the relative amount of electrons with a binding energy matching that of the X-rays scales with the electron density. Hence materials with a high density and high atomic number interact strongly, while low density and low atomic number materials interact weakly. This material sensitivity has made X-rays transmission imaging applicable in medical analysis, as bone absorbs most of the radiation while soft tissue lets it pass.

The limiting factor of X-ray transmission imaging has been its inability to image weakly absorbing objects. Due to this, another X-ray imaging technique can be deployed, particularly propagation-based X-ray phase-contrast imaging PB-PCI. In this imaging technique, the object exit-wave is allowed to propagate behind the sample. The propagation distance increases edge contrast, as near-field phase interference of the propagated radiation gives rise to distinct sharp intensity features at the interface between two materials. This is especially useful for low contrast features comprised of materials with a low atomic number and density (e.g. organic samples).

For cases where an object displays intricate geometrical structures, three-dimensional analysis is beneficial, and then X-ray tomography can be utilized. This imaging method works by collecting a set of images for an object at different angles. These images, more commonly called projections, are associated with a specific angular view of the object. By rotating the object around a centre point and acquiring a set of angular equidistant projections between $0° \to 180°$, the 3d information of the object can be retrieved. The reason for this can qualitatively be explained when viewing the process in terms of a cylindrical coordinate system. Here each projection will span a planar view of the object space for a specific angular position, and as the projections span angles between $0° \to 180°$, the whole object space can be filled. When combining tomography with PB-PCI, the technique can also be deployed to make structural analysis of complex organic structures. Consequently, propagation-based X-ray phase-contrast tomography PB-PCT has seen a high adoption rate in areas of biological, medical and material research [1, 2, 3].

The phase contrast induced by the interference effects are generally not ideal, and the real spatial information of an object is of interest. Hence phase retrieval algorithms have been developed to correct for these phase interference effects [4]. These algorithms have predominately been applied as a 2d filter on the projections. However, recent results have shown the possibility of applying the phase correction in localized regions of the reconstructed 3d volume [5]. The 3d phase retrieval approach includes additional approximations to the in-line contrast function utilizing the constraint of a weak phase object, which is ordinarily justified. However, samples composed of long straight features, as encountered in the cellular structure of wood, could invalidate this constraint.

Therefore, a closer investigation of how long straight features displays phase contrast is of importance, as it could potentially exhibit unknown effects. Furthermore, the comparison between 3d phase retrieval and 2d phase retrieval has seen minimal testing in lab-based settings where samples often are larger, which could increase the differentiation between the two methods. Thus by combining the rectangular features with the phase retrieval

comparison, an unexplored area will hopefully be revealed.

By simulating PB-PCT for a rectangular cuboid, section 4.1, we show that sharp edges give rise to phase fringe artefacts. Additionally, the rapid changes in integrated thickness for the projections appear to increase the reconstruction errors. A defect that to our knowledge only has been documented in transmission tomography [6]. Including these artefacts, the discrepancy in the intensity terms coming from the approximated in-line contrast function remained within tolerable levels at the phase fringes for organic materials, re-enforcing the current consensus. The 2d and 3d phase retrieval approaches were also compared, showing similar results.

Laboratory measurements were also done on a wood splinter, section 4.2, to verify the existence of the issues encountered in the simulations. These could not give quantifiable evidence of the defect due to external alignment problems but qualitatively showed an overall decreased contrast. The phase retrieval methods were also applied to one of the datasets and showed a larger difference in the retrieved contrast compared to the simulation but maintained the same feature size for both. Due to the external alignment problems for the laboratory measurements, another simulation using a segmented wood splinter as a phantom and following the same experimental methodology as the laboratory measurements. The same decreased contrast could be shown, including a quantifiable comparison between phase fringes, revealing a feature size discrepancy.

2   Theory
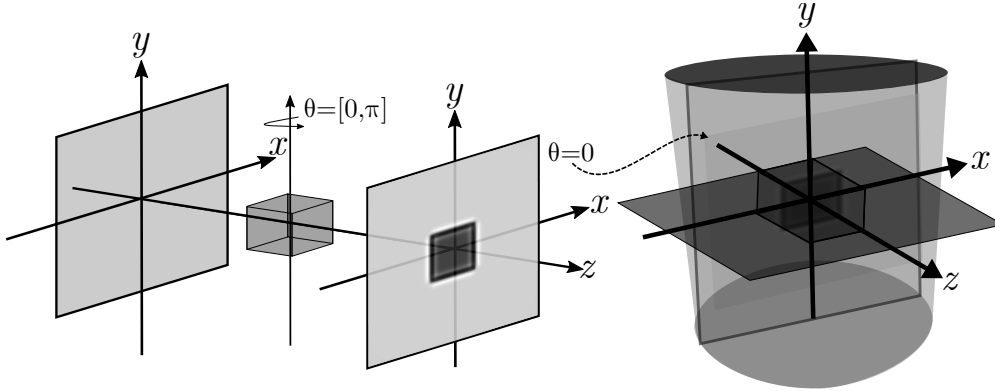
Figure 1: A propagation-based phase-contrast image taken at $\theta = 0$, resulting in qualitatively acquiring a plane spanning the object space for that angle.

This thesis will predominately revolve around the numerical implementation of PB-PCT and 3d phase retrieval. As such, the underlying theoretical framework needs careful consideration. We will start by introducing the physics around propagation-based phase-contrast imaging and then move on to the fundamentals of tomography, followed by phase retrieval. The first sections in propagation-based phase-contrast imaging will contain the description of a pure light field and its spectral decomposition into monochromatic components. These are then separately propagated, though the propagation is restricted to vacuum and forward propagating fields.

Constraints are then further imposed on the light to be paraxial, resulting in Fresnel diffraction. This limited form of propagation is extended to interactions with matter, where phase interference effects manifest after the object-perturbed wave field propagates, fig. 1. The effects of a lab-based source are explained, and finally included with the detector response to the radiation in the optical transfer function.

In the tomography section, we will first start with the introduction of the Radon transform. This transform creates a direct link between the acquired projected spatial information and the Fourier domain. However, due to discrete angular sampling, the inverse Radon transform creates reconstruction artefacts. To overcome these issues the filtered back projection algorithm will be derived utilizing the Radon transform. Lastly, we will formulate the theory behind two and three- dimensional TIE phase retrieval.

2.1 Propagation-based phase-contrast imaging

2.1.1 Spectral decomposition

The propagation of pure light fields can in many cases be too arduous to work with directly. Therefore light fields are often expressed as a superposition of monochromatic fields, as this can levitate some of the immediate complexity. To that end, we assume a complex scalar light field function of the form $\Psi(x, y, z, t)$ that lie within a limited volume of free space, i.e. a perfect vacuum. This function is spectrally decomposed via the Fourier integral as a superposition of monochromatic fields,

$$\Psi(x, y, z, t) = \frac{1}{\sqrt{2\pi}} \int_0^\infty \psi(x, y, z) e^{-i\omega t} d\omega \tag{1}$$

Here $\psi(x, y, z)$ and $e^{-i\omega t}$ represents the spatial and temporal factors in the monochromatic components respectively. Additionally, the decomposing integral only includes positive angular frequencies ω, allowing for another analytic formulation, as the time variable t for the wave-function $\Psi(x, y, z, t)$ can be chosen as a complex number [7].

Now, attention is turned to the evolution of the monochromatic spatial components of the decomposed wave-function via substitution of eq. (1) into the d'Alembert wave equation,

$$\left(\frac{1}{c^2}\frac{\partial^2}{\partial t^2} - \nabla^2\right)\Psi(x, y, z, t) = 0 \implies \left(\frac{1}{c^2}\frac{\partial^2}{\partial t^2} - \nabla^2\right)\frac{1}{\sqrt{2\pi}}\int_0^\infty \psi(x, y, z)e^{-i\omega t}d\omega = 0 \tag{2}$$

$$\implies \frac{1}{\sqrt{2\pi}}\int_0^\infty \left[\left(\frac{(-i\omega)^2}{c^2} - \nabla^2\right)\psi(x, y, z)\right]e^{-i\omega t}d\omega = 0$$

$$\implies \frac{-1}{\sqrt{2\pi}}\int_0^\infty \left[\left(\nabla^2 + \frac{\omega^2}{c^2}\right)\psi(x, y, z)\right]e^{-i\omega t}d\omega = 0 \tag{3}$$

From this point, it is clear that the monochromatic spatial components must vanish. Resulting in a time-independent equation, the so-called Helmholtz equation,

$$\left(\nabla^2 + k^2\right)\psi(x, y, z) = 0, \qquad k = \frac{w}{c} \tag{4}$$

where k is the angular wavenumber and c the speed of light in vacuum.

2.1.2 Forward propagating fields

The general form of propagation for a monochromatic component is handled by the Helmholtz equation. However, to get a simpler picture of the problem we restrict our formulation to only include propagation which is going in the positive optical direction, meaning that the wave is no longer able to propagate backwards. We also try to look at a one solution to the Helmholtz equation, namely the elementary plane waves, to gain some useful insights.

Using the aforementioned restriction we can further the derivation by presuming a wave-field to be forward propagating along the $z-$axis, where the magnitude of a single monochromatic component is known. By the angular spectrum formalism the initial disturbance can be used to acquire the propagated disturbance further downstream at $z > 0$. We therefore choose a Cartesian coordinate system (x, y, z), where the positive z-axis is the nominal optical axis. The two planes $z = 0$ and $z = \Delta, \Delta > 0$ are assumed to be parallel with vacuum in-between [7], for a visual representation see fig. 2.

Turning the attention to a simple solutions for the Helmholtz equation, the elementary plane waves,

$$\Phi(x, y, z) = e^{i(k_x x + k_y y + k_z z)}, \qquad k^2 = k_x^2 + k_y^2 + k_z^2, \qquad |k| = \frac{2\pi}{\lambda} \tag{5}$$

we can see how a simple disturbance will behave through propagation. As the wave-field is propagating along the $z-$axis, we chose to solve the wave vector for this direction k_z,

$$k_z = \sqrt{k^2 - k_x^2 - k_y^2} \tag{6}$$

Reminding ourselves that the wave-field is restricted to be forward-propagating, thus the only solutions to k_z which are valid, are the ones which are strictly positive and real. As such, the elementary plane waves can take the form of,

$$\Phi(x, y, z) = e^{i(k_x x + k_y y)} e^{iz\sqrt{k^2 - k_x^2 - k_y^2}} \tag{7}$$

for which the boundary $z = 0$ is,

$$\Phi(x, y, z = 0) = e^{i(k_x x + k_y y)} \tag{8}$$

Now it can be seen that the propagated disturbance $\Phi(x, y, z > 0)$ will be the unpropagated disturbance $\Phi(x, y, z = 0)$ times the propagation factor $e^{iz\sqrt{k^2 - k_x^2 - k_y^2}}$ or more commonly, the free space propagator.

With the new found information, we turn back to the general solution of the Helmholtz equation and try to evaluate its disturbance at $z = \Delta$. Starting by taking the two-dimensional Fourier integral of $\psi(x, y, z = 0)$,

$$\psi(x, y, z = 0) = \frac{1}{2\pi} \iint \hat{\psi}(k_x, k_y, z = 0) e^{i(k_x x + k_y y)} dk_x dk_y \tag{9}$$

for which $\hat{\psi}(k_x, k_y, z = 0)$ represents the Fourier transform of $\psi(x, y, z = 0)$. Subsequently, the initial wave-field is now decomposed to a linear combination of plane waves, each of which

solves the Helmholtz equation in the same way as before. Thus multiplying each plane wave component with the free space propagator the desired outcome is retrieved,

$$\psi(x, y, z = \Delta) = \frac{1}{2\pi} \iint \hat{\psi}(k_x, k_y, z = 0) e^{i(k_x x + k_y y)} \cdot e^{i\Delta\sqrt{k^2 - k_x^2 - k_y^2}} dk_x dk_y \qquad (10)$$

This way of retrieving the propagated wave-field is referred to as the angular-spectrum representation. However, for simplicity we also state the free-space propagator as a diffraction operator $\mathcal{D}_\Delta$ which acts on the initial field [7],

$$\psi(x, y, z = \Delta) = \mathcal{D}_\Delta \psi(x, y, z = 0) \implies \mathcal{D}_\Delta = \mathcal{F}^{-1} e^{i\Delta\sqrt{k^2 - k_x^2 - k_y^2}} \mathcal{F}, \qquad \Delta \geq 0 \qquad (11)$$
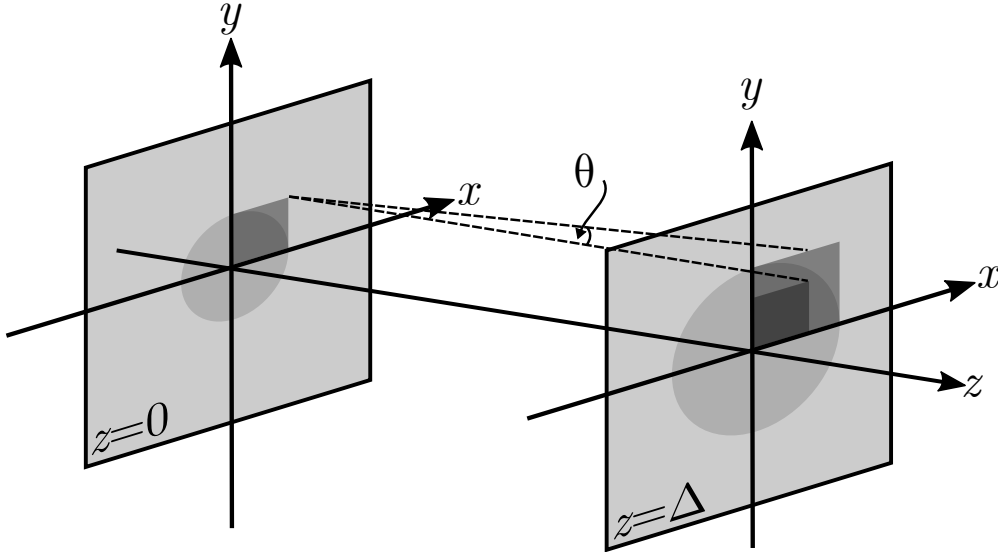
2.1.3 Fresnel diffraction

Figure 2: A view of the forward propagating wave-field going along the z-axis. The dashed line represents a X-ray ray path going trough the vacuum region $z = [0, \Delta]$, θ depicts the angle from the optical path in the z direction. For the paraxial approximation to be valid this angle would be small.

So far the angular spectrum formalism has only been used to formulate the free-space propagation of a coherent scalar field between parallel planes. However, we further limit ourselves, by assuming that the X-rays follow a paraxial path, fig. 2. Meaning that the rays can only have a small angle θ from the optical axis, such that,

$$\sin(\theta) \approx \theta, \qquad \tan(\theta) \approx \theta, \qquad \cos(\theta) \approx 1 \qquad (12)$$

This implicitly means that plane-wave components for $|k_x|, |k_y|$ will be much less than $|k_z|$, once $z \geq 0$. Hence eq. (6) can be approximated with the binomial approximation as,

$$k_z \approx k - \frac{k_x^2 + k_y^2}{2k} \qquad (13)$$

8

which in turn allows for a reformulation of the diffraction operator $\mathcal{D}_\Delta$ as the Fresnel diffraction operator $\mathcal{D}_\Delta^F$,

$$\mathcal{D}_\Delta \approx \mathcal{D}_\Delta^F = e^{ik\Delta}\mathcal{F}^{-1}e^{\frac{-i\Delta\left(k_x^2+k_y^2\right)}{2k}}\mathcal{F} \implies \tag{14}$$

$$\psi(x,y,z=\Delta) = \mathcal{D}_\Delta^F\psi(x,y,z=0) = e^{ik\Delta}\mathcal{F}^{-1}e^{\frac{-i\Delta\left(k_x^2+k_y^2\right)}{2k}}\mathcal{F}\psi(x,y,z=0) \tag{15}$$

Note that $e^{ik\Delta}$ is a constant phase term and will have no effect on the intensity and is in many cases ignored [7].

Furthermore, one commonly uses the dimensionless Fresnel number N_F to described which diffraction theory correctly describes the diffraction approximations. That being either Fraunhofer diffraction describing the far-field and Fresnel diffraction the near-field. The Fresnel number can be defined by assuming an unpropagated disturbance at $z=0$ which exists only over a diameter a

$$N_F = \frac{ka^2}{2\pi\Delta} \tag{16}$$

Then if the propagation distance Δ is large we have $N_F \ll 1$ and we subsequently are in the far field, and if the propagation distance Δ is small, $N_F \geq 1$, we are in the near-field [8].

2.1.4 The projection approximation
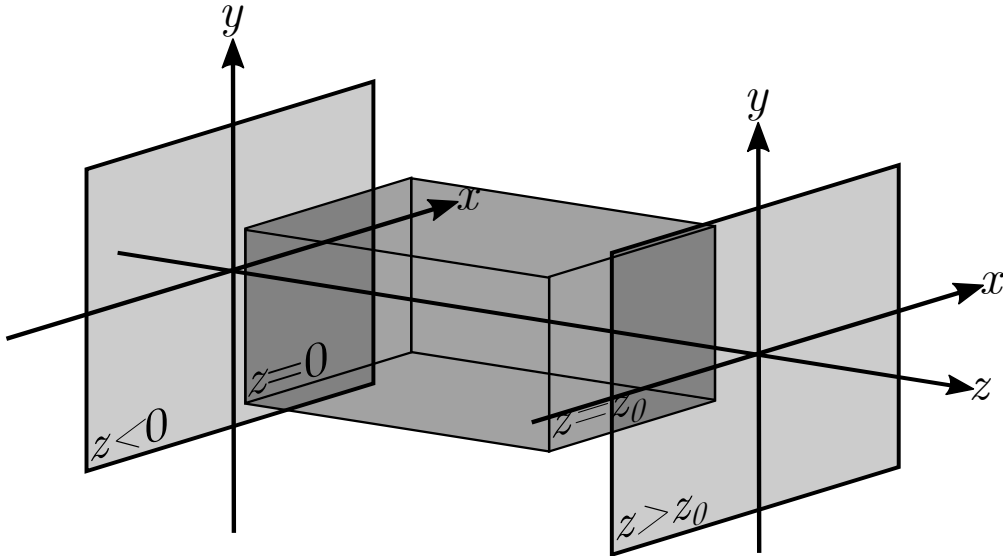
Figure 3: A schematic of the projection approximation, where a non-magnetic weakly scattering objects is located between the regions $z = [0, z_0]$, while the half spaces $z \leq 0$ and $z \geq z_0$ consist of vacuum.

X-ray imaging exclusively revolves around matter, however, up till now propagation has only occurred in a vacuum. We, therefore, start by assuming that our complex scalar light field function $\Psi(x,y,z,t)$ lies within a limited volume containing a non-magnetic material[1].

---

[1]This is a good approximation even for magnetic materials given that lab-sources generally produces unpolarized light.

Correspondingly the d'Alembert wave equation no longer holds, and instead, the disturbance obeys,

$$\left(\epsilon(x,y,z)\mu_0\frac{\partial^2}{\partial t^2} - \nabla^2\right)\Psi(x,y,z,t) = 0 \tag{17}$$

Using the same decomposition as in section 2.1.1 and substituting into eq. (17) the following is obtained,

$$\frac{-1}{\sqrt{2\pi}}\int_0^\infty \left[\left(\nabla^2 + \epsilon(x,y,z)\mu_0\omega^2\right)\psi(x,y,z)\right]e^{-i\omega t}d\omega = 0 \tag{18}$$

Again the spatial part must vanish independently of time,

$$\left(\nabla^2 + \epsilon(x,y,z)\mu_0c^2k^2\right)\psi(x,y,z) = 0, \qquad ck = \omega \tag{19}$$

Noting that $\epsilon(x,y,z)\mu_0c^2$ equals the square of the refractive index $n(x,y,z)$ for a non-magnetic material,

$$n(x,y,z) = \sqrt{\epsilon_r\mu_r} = \sqrt{\frac{\epsilon(x,y,z)}{\epsilon_0}\cdot 1}, \implies \tag{20}$$

$$\epsilon(x,y,z)\mu_0c^2 = \frac{\epsilon(x,y,z)}{\epsilon_0} = n^2(x,y,z), \qquad c = \frac{1}{\sqrt{\epsilon_0\mu_0}} \tag{21}$$

one arrives at the Helmholtz equation for a inhomogeneous medium,

$$\left(\nabla^2 + n^2(x,y,z)k^2\right)\psi(x,y,z) = 0 \tag{22}$$

Additionally, by virtue of the linearity from eq. (17), we implicitly have that distinct angular frequencies are uncoupled [7]. The direct result of this means that inelastic scattering is undescribed within the considered model. However, because of the specified energy regime of $E < 50$ keV, inelastic scattering cross-sections will remain small.

The regions $z \leq 0$ and $z \geq z_0$ again consist of vacuum while the space between $0 < z < z_0$ is comprised of a non-magnetic weakly scattering object as in fig. 3. Due to the object being weakly scattering, the wave-field will only perturb slightly by propagating through it. Thus the incident perturbed plane wave $\psi(x,y,z)$ can be expressed as an unscattered plane wave e^{ikz}, and an envelop function $\tilde{\psi}(x,y,z)$ where the envelop and field have the same intensity,

$$\psi(x,y,z) \equiv \tilde{\psi}(x,y,z)e^{ikz}, \qquad |\psi(x,y,z)|^2 = |\tilde{\psi}(x,y,z)|^2 \tag{23}$$

Insert the above into eq. (22)

$$\left(\nabla^2 + n^2(x,y,z)k^2\right)\tilde{\psi}(x,y,z)e^{ikz} = 0 \implies \tag{24}$$

$$\left(\tilde{\psi}(x,y,z)\nabla^2 e^{ikz} + e^{ikz}\nabla^2\tilde{\psi}(x,y,z) + 2\nabla\tilde{\psi}(x,y,z)\nabla e^{ikz} + n^2(x,y,z)k^2\tilde{\psi}(x,y,z)e^{ikz}\right) = 0$$

$$\implies \left((ik)^2 e^{ikz} + e^{ikz}\nabla^2 + 2ike^{ikz}\frac{\partial}{\partial z} + n^2(x,y,z)k^2 e^{ikz}\right)\tilde{\psi}(x,y,z) = 0$$

Drop the linear phase factor e^{ikz} and rewrite the Laplacian ∇^2 via its transverse component $\nabla^2_\perp$ in xy. This is possible as our field is paraxial, allowing us to ignoring the second derivative in the z direction.

$$\left(2ik\frac{\partial}{\partial z} + \nabla^2_\perp + k^2(n^2(x,y,z) - 1)\right)\tilde{\psi}(x,y,z) = 0 \tag{25}$$

By the essence of the projection approximation, the transverse Laplacian can largely be ignored, as the object does not provide sufficiently large scattering for the rays to deflect from their original path. The envelope at $z = z_0$, it will be set by the phase and amplitude shifts that occurred during the propagation in the object. Finally, rearranging results in the partial differential equation,

$$\frac{\partial}{\partial z}\tilde{\psi}(x,y,z) \approx \frac{k}{2i}\left(1 - (n^2(x,y,z)\right)\tilde{\psi}(x,y,z) \tag{26}$$

and solving the boundary value problem one obtains,

$$\tilde{\psi}(x,y,z=z_0) \approx e^{\frac{k}{2i}\int_{z=0}^{z=z_0}\left(1-(n^2(x,y,z))\right)}\tilde{\psi}(x,y,z=0) \tag{27}$$

Here we use that the refractive index in the X-ray regime is usually denoted by its complex form,

$$n = 1 - \delta + i\beta \tag{28}$$

where both δ and β are real numbers much smaller than one. Hence a first order evaluation of the term $(1 - (n^2(x,y,z))$ is valid and gives,

$$\left(1 - (n^2(x,y,z))\right) \approx 2\left(\delta(x,y,z) - i\beta(x,y,z)\right) \tag{29}$$

Consequently, we arrive at the final result,

$$\tilde{\psi}(x,y,z=z_0) \approx e^{-ik\int_{z=0}^{z=z_0}(\delta(x,y,z)-i\beta(x,y,z))dz}\tilde{\psi}(x,y,z=0) \tag{30}$$

A interesting remark is that the phase shift $\Delta\phi(x,y)$ for the weakly scattering object is given by,

$$\Delta\phi(x,y) = -k\int\delta(x,y,z)dz \tag{31}$$

If the object is strictly comprised of a single material, the phase shift can be simplified by taking the projected thickness $T(x,y)$ along the optical axis, resulting in,

$$\Delta\phi(x,y) = -k\delta T(x,y) \tag{32}$$

Now identifying the squared modulus of eq. (30),

$$I(x,y,z=z_0) = e^{-2k\int_{z=0}^{z=z_0}\beta(x,y,z)dz}I(x,y,z=0) \tag{33}$$

it becomes apparent that for a single material object this reduces to Beer's law of absorption,

$$I(x,y,z=z_0) = e^{-\mu T(x,y)}I(x,y,z=0) = e^{-\mu T(x,y)}I^{in}, \qquad \mu = 2k\beta \tag{34}$$

where μ is the linear attenuation coefficient [7].
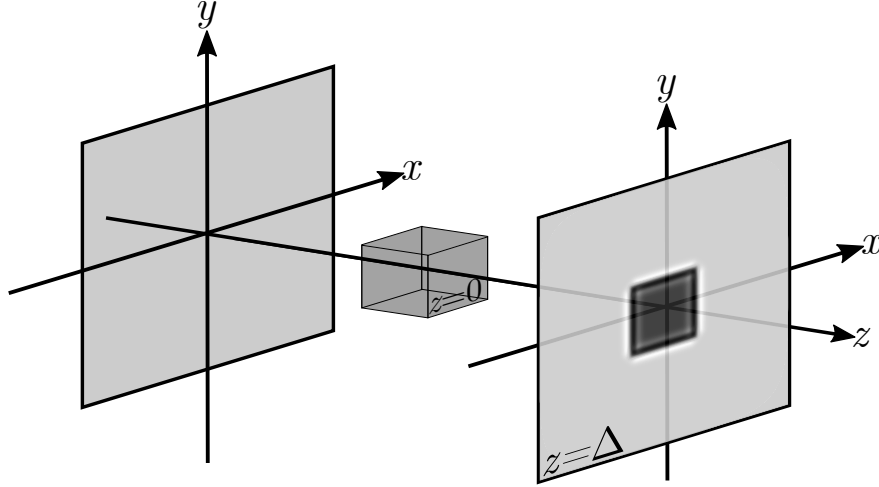
2.1.5 Propagation-based phase contrast

Figure 4: In the idealized case of propagation-based phase contrast the phase variations occurring in the weakly scattering object gives rise to intensity shift in the measured image.

Up to now, the theory for near-field propagation has briefly been reviewed. However, to readably show how phase variations induced by free-space propagation gives rise intensity variations on a detector plane, some further approximations are needed. Consider a weakly scattering object that is being illuminated along the z-axis with paraxial monochromatic scalar electromagnetic radiation, as depicted in fig. 4. The exit-surface plane which we say to exist over $z = 0$ will be,

$$\psi(x, y, z = 0) = \sqrt{I(x, y, z = 0)} e^{i\phi(x,y,z=0)} \tag{35}$$

where $\sqrt{I(x, y, z = 0)}$ and $\phi(x, y, z = 0)$ are the intensity and phase of the radiation over said plane. Also, infer that the propagation distance Δ is small enough that the second-order Taylor expansion approximates the second exponent in the Fresnel propagator, see eq. (15),

$$e^{\frac{-i\Delta\left(k_x^2 + k_y^2\right)}{2k}} \approx 1 - \frac{i\Delta\left(k_x^2 + k_y^2\right)}{2k} \tag{36}$$

Now substitute eq. (36) and eq. (35) into eq. (15) and exert the Fourier derivative theorem, for which we obtain the propagated wave-field at $z = \Delta$,

$$\psi(x, y, z = \Delta) = e^{ik\Delta}\left(1 + \frac{i\Delta\nabla_\perp^2}{2k}\right)\sqrt{I(x, y, z = 0)} e^{i\phi(x,y,z=0)} \tag{37}$$

Furthermore, given that we would like to know the intensity at the detector plane we take the modulus squared of the propagated wave-field. Here the quadratic propagation distances Δ terms are disregard, as they are sufficiently small.

$$I(x, y, z = \Delta) = I(x, y, z = 0)$$
$$+ 2\text{Re}\left[\sqrt{I(x, y, z = 0)}e^{i\phi(x,y,z=0)}\frac{i\Delta}{2k}\nabla_\perp^2\sqrt{I(x, y, z = 0)}e^{i\phi(x,y,z=0)}\right] \implies \tag{38}$$

$$I(x, y, z = \Delta) = I(x, y, z = 0) - \frac{\Delta}{k} \nabla_\perp \left[I(x, y, z = 0) \nabla_\perp \phi(x, y, z = 0) \right] \qquad (39)$$

This final equation is referred to as the transport-of-intensity equation and is of high importance due to its use in many phase retrieval algorithms [7].
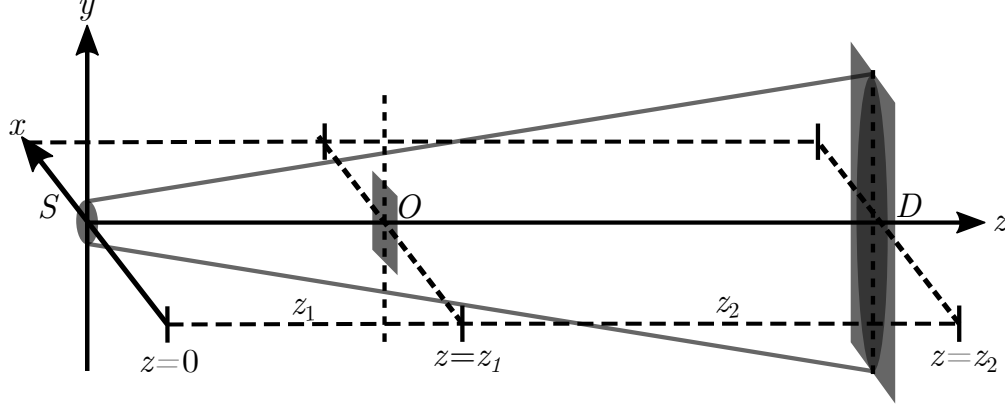
2.1.6 Fresnel scaling

Figure 5: In a cone-beam geometry, a monochromatic divergent point source is located at the point S. The source S, in turn, emits X-rays further downstream in the positive z direction hitting a weakly scattering object at O for which an exit wave is produced at z_1. This exit wave then propagates in free space towards the detector plane D at z_2 where a Fresnel diffraction pattern is measured. As a result of the cone-beam, the image will be a magnified by a factor M, given by $\frac{z_1+z_2}{z_1}$.

In lab-based imaging, an extended source with a defined size produces quite divergent X-rays and consequently requires appropriate detector intensity scaling. To fix the divergence effects, we can use a cone-beam geometry to retrieve the effective propagation distance z_{eff} [9]. However, to account for the source size, we will in a later section 2.1.7, develop a simplistic way to apply the blurring effects across the detector plane resulting from the finite size.

Going back to the problem of divergence, we can use the geometry from fig. 5, where S denotes the divergent point source which produces monochromatic scalar X-ray waves. The entire system is as in the previous sections surrounded by vacuum, and the propagation occurs along the optical axis chosen as z. The source is located downstream from a weakly scattering object O by a distance z_1 which is far enough away to allow for the X-rays to be paraxial at the object surface. As for the object, it is a distance z_2 from the detector D, and the total propagation distance from the source to the detector is thus $z_{tot} = z_1 + z_2$.

Further assume that Fresnel diffraction is valid between the object exit wave $\psi(x, y, z = z_1)$ and the wave hitting the detector $\psi(x, y, z = z_2)$. Start by rewriting the Fresnel diffraction in terms of its convolutional formulation, the Fresnel diffraction integral [7],

$$\psi(x, y, z = z_2) = \frac{-ike^{ikz_2}}{2\pi z_2} e^{\frac{ik}{2z_2}(x^2+y^2)}.$$

$$\iint_{-\infty}^{\infty} \psi(x', y', z = z_1) e^{\frac{ik}{2z_2}(x'^2+y'^2)} e^{\frac{-ik}{z_2}(xx'+yy')} dx'dy' \qquad (40)$$

13

Given that our object is weakly scattering the projection approximation can be used. Combine this with the paraxial approximation, then the exit wave for point-source illumination $\psi(x, y, z = z_1)$, can be described as an exit wave by plane-wave illumination $\psi^\infty(x, y, z = z_1)$ via,

$$\psi(x, y, z = z_1) = \psi^\infty(x, y, z = z_1)e^{\frac{ik}{2z_1}(x^2+y^2)} \tag{41}$$

substitute eq. (41) into eq. (40),

$$\psi(x, y, z = z_2) = \frac{-ike^{ikz_2}}{2\pi z_2}e^{\frac{ik}{2z_2}(x^2+y^2)}.$$
$$\iint_{-\infty}^{\infty} \psi^\infty(x', y', z = z_1)e^{\frac{ik}{2}\left(\frac{1}{z_2}+\frac{1}{z_1}\right)(x'^2+y'^2)}e^{\frac{-ik}{z_2}(xx'+yy')}dx'dy' \tag{42}$$

Now introduce the geometrical magnification M given by the ratio between the total propagation distance and the source-to-sample distance,

$$M = \frac{z_{tot}}{z_1} = \frac{z_1 + z_2}{z_1} \tag{43}$$

and the effective propagation distance z_{eff},

$$\frac{1}{z_{eff}} = \frac{1}{z_2} + \frac{1}{z_1} = \frac{1}{z_2}\left(\frac{z_1 + z_2}{z_1}\right) = \frac{M}{z_2} \tag{44}$$

Use eq. (44) and take the squared modulus of eq. (42), i.e. the intensity at the detector.

$$I(x, y, z = z_2) = \frac{k^2}{4\pi^2 z_2^2}\left|\iint_{-\infty}^{\infty} \psi^\infty(x', y', z = z_1)e^{\frac{ikM}{2z_2}(x'^2+y'^2)-\frac{ik}{z_2}(xx'+yy')}dx'dy'\right|^2 \tag{45}$$

To check the validity of our derivation we go the limit $z_1 \to \infty$ where $M = 1$ and we have parallel beam,

$$I^\infty(x, y, z = z_2) = \frac{k^2}{4\pi^2 z_2^2}\left|\iint_{-\infty}^{\infty} \psi^\infty(x', y', z = z_1)e^{\frac{ik}{2z_2}(x'^2+y'^2)-\frac{ik}{z_2}(xx'+yy')}dx'dy'\right|^2 \tag{46}$$

Here we return at the intensity given by Fresnel diffraction. Furthermore, comparing the two equations eq. (45) and eq. (46) directly we get the Fresnel scaling theorem [7].

$$I(x, y, z = z_2) = \frac{1}{M^2}I^\infty\left(\frac{x}{M}, \frac{y}{M}, z = \frac{z_2}{M}\right) \tag{47}$$
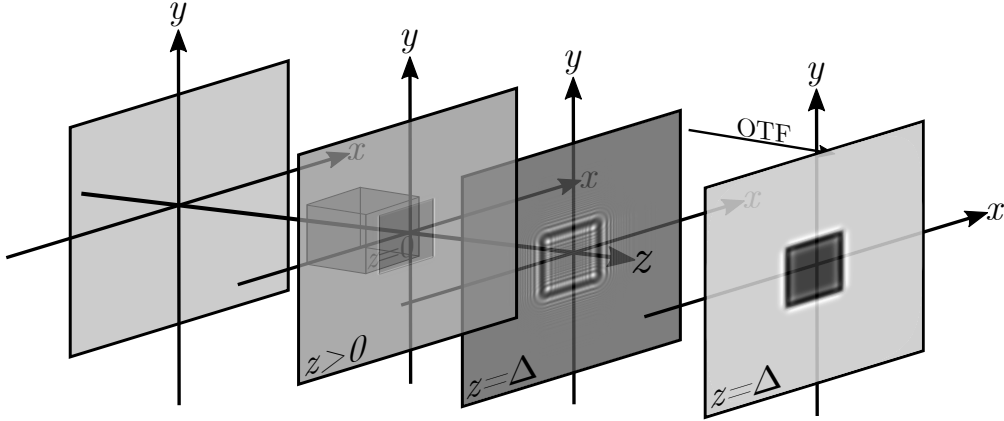
14

2.1.7 The optical transfer function

Figure 6: For a small propagation distance where $0 < z < \Delta$ the near-field approximation can be well described by the use of TIE. However, when the propagation distance becomes large enough $z = \Delta$ this approximation no longer holds. Instead, it will be appropriately evaluated via free-space propagation, meaning that the measured image will occupy the holographic regime, containing higher-order phase fringes. As a result of the limited resolution from the X-ray source and the detector, the image will be blurred, thus losing the higher-order fringes.

The idealized case of propagation-based X-ray imaging is a useful tool for simulation, but as in most cases will not reflect a realistic picture. Instead, the blurring effects ruled by the X-ray source and the detector restrict the resolution. To that end, the optical transfer functions describing this behaviour will be introduced. However, here we will limit ourselves to a simplistic picture where its existence is explained without any rigorous derivation.

Suppose that the source takes the form of an X-ray tube where high energy electrons are bombarded onto a metal anode creating a spectrum of X-rays. This spectrum is partially composed of bremsstrahlung radiation, producing a broad spectrum. Superimposed on top of this is much stronger characteristic line profiles of the fluorescent radiation due to electron collisions with the target atoms [10]. The produced X-ray will also be incoherent as the rays are in no way correlated to each other. Nonetheless, using a small pinhole and only letting through a subset of the rays, a more coherent source can be formed.

As a result, the source can no longer be viewed as a perfect point source but instead as an extended source of size d. Given that it still keeps with the small-angle approximation, each point on the new area source will give an identical image of the object. However, there will be a small translation at the detector plane resulting in an blurring effect.

The effect can be describe as a convolution with the source spatial distribution

$$I(x, y, z = z_2) = \iint I(x', y', z = 0) \frac{1}{(M-1)^2} A\left(\frac{x'-x}{M-1}, \frac{y'-y}{M-1}\right) dx' dy' \qquad (48)$$

here $A(x, y)$ denotes the source brightness which is normalized to one [11]. This can then be combined with the results obtained in eq. (30) and eq. (15) to yield the blurred intensity I_B of the object after free-space propagation,

$$I_B = \mathcal{F}^{-1}\left[\mathcal{F}\left(\left|\mathcal{D}_\Delta^F \psi(x, y, z = z_1)\right|^2\right) \cdot \mathcal{F}\left(\frac{1}{(M-1)^2} A\left(\frac{x'-x}{M-1}, \frac{y'-y}{M-1}\right)\right)\right] \qquad (49)$$

where $\psi(x, y, z = z_1)$ is the object exit wave.

While this creates a more realistic final evaluation, there is still the detector response to the radiation. The idea is that each photon has a high chance of interacting with more than one pixel on the imaging device. This effect intrinsically reduces the resolution by forming additional blurring. The blurring, can by the same idea as before, be calculated through the convolution of the point spread function (PSF).

This function describes the distribution of the signal from the incident X-rays on a single detector point. To note is that the PSF is sometimes interchangeably used with the detector modulation transfer function (MFT), this is because it equals the Fourier transform of the point spread function, $\text{MFT} = |\mathcal{F}(\text{PSF})|$.

Hence by convoluting the these two blurring effects we can describe the optical transfer function (OTF) of the system,

$$\text{OTF} = \text{MFT} \cdot \mathcal{F} \left(\frac{1}{(M-1)^2} A \left(\frac{x' - x}{M - 1}, \frac{y' - y}{M - 1} \right) \right) \tag{50}$$

for which we obtained the final blurred intensity as,

$$I_B = \mathcal{F}^{-1} \left[\mathcal{F} \left(\left| \mathcal{D}_\Delta^F \psi(x, y, z = z_1) \right|^2 \right) \cdot \text{OTF} \right] \tag{51}$$

Another result of the blurring effects is that the feature size a, in the Fresnel number eq. (16), can be expressed in terms of the system resolution and the magnification geometry [12]. Resulting in an extended near-field regime given that "feature size" is restricted by the resolution of the system. Furthermore, as seen in fig. 6, the image ideally occupies the holographic regime at $z = \Delta$ and subsequently contains higher-order fringes. Although as mentioned before the resolution is limited by the OTF. Meaning that these higher-order terms are lost, and instead the final image is a broad near-field image.

2.2 Tomography

2.2.1 Radon transform

With the fundamentals of propagation-based phase-contrast imaging in place, one would now like to spend some time on how to obtain the refractive index of a three-dimensional object. The general idea is quite straight forward, take a two-dimensional image containing the projected index of refraction of the object. Then rotate the object by a number of rotation angles θ, and collect an image for each rotation. Use this set of projections to reconstruct the 3d object.

To that end, let (x', y', z') denote the coordinate system of the laboratory frame of reference and (x, y, z) the object frame as in fig. 7, in which the laboratory frame can be rotated clockwise by the angle θ [13],

$$\begin{pmatrix} x' \\ y' \\ z' \end{pmatrix} = \begin{pmatrix} \cos(\theta) & 0 & \sin(\theta) \\ 0 & 1 & 0 \\ -\sin(\theta) & 0 & \cos(\theta) \end{pmatrix} \begin{pmatrix} x \\ y \\ z \end{pmatrix} \tag{52}$$
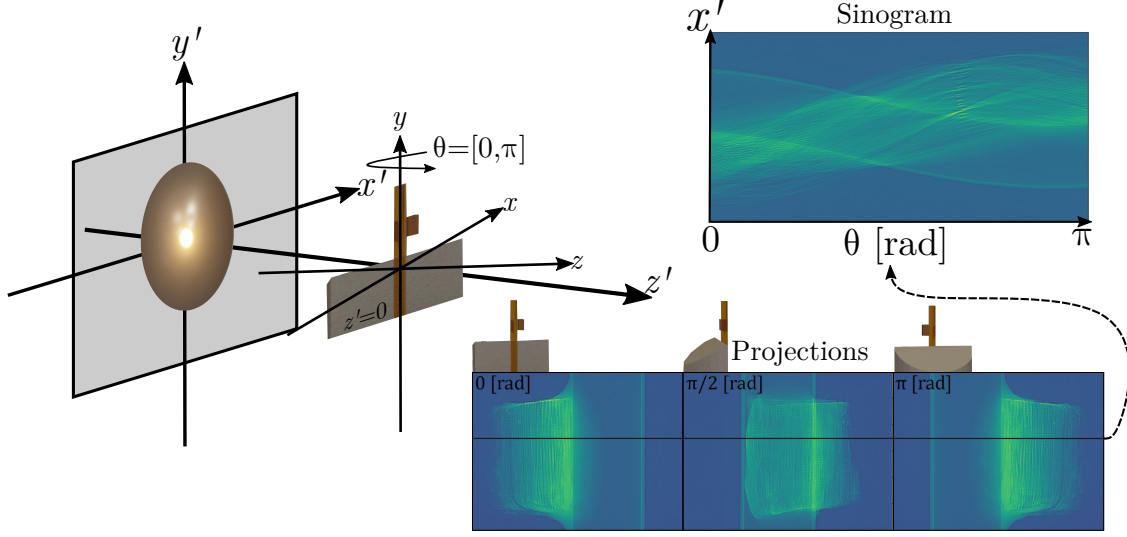
Figure 7: To extract the original object $f(x, y, z)$, a set of tomographic projections are collected $p_\theta(x', y')$. If the y' component is locked on to a single value, as depicted with the black line the projections, a sinogram can be formed. The sinogram shows the set of Radon transform for all projection angles $\theta = [0, \pi]$, which creates the basis for the filter back projection algorithm.

Like before, assume a forward propagating beam along the z' direction. Next, consider a function $f(x, z)$ which describes either the real δ or complex β part of the refractive index for a constant y value, meaning one slice through the 3d volume. The projection $p_\theta(x')$ of this function for a certain rotation angle θ will then be given by,

$$
\begin{aligned}
p_\theta(x') = \mathcal{R}_\theta f(x') &= \int_{\mathbb{R}} f(x, z) dz' \\
&= \int_{\mathbb{R}} f(x' \cos(\theta) - z' \sin(\theta), x' \sin(\theta) + z' \cos(\theta)) dz' \\
&= \int_{\mathbb{R}^2} f(x, z) \delta_D(x \cos(\theta) + z \sin(\theta) - x') dx dz
\end{aligned}
\tag{53}
$$

where $\mathcal{R}_\theta$ denotes the two-dimensional Radon transform and δ_D the Dirac delta distribution [13]. As a result, the Radon transform is the integration over the lines going along z' with length x' from the origin. If only a single point located at (x_0, z_0) with an associated function $f(x, z) = \delta_D(x - x_0)\delta_D(z - z_0)$ is considered, the Radon transform of the point will be,

$$
\begin{aligned}
\mathcal{R}_\theta f(x') &= \int_{\mathbb{R}} \delta_D(x' \cos(\theta) - z' \sin(\theta) - x_0)\delta_D(x' \sin(\theta) + z' \cos(\theta) - z_0) dz' \\
&= \frac{1}{|\cos(\theta)|} \int_{\mathbb{R}} \delta_D(x' \cos(\theta) - z' \sin(\theta) - x_0)\delta_D\left(z' - \left(\frac{z_0}{\cos(\theta)} - \frac{x' \sin(\theta)}{\cos(\theta)}\right)\right) dz' \\
&= \frac{1}{|\cos(\theta)|} \delta_D\left(x' \cos(\theta) - \left(\frac{z_0}{\cos(\theta)} - \frac{x' \sin(\theta)}{\cos(\theta)}\right)\sin(\theta) - x_0\right) \\
&= \delta_D(x' - \sin(\theta)z_0 - \cos(\theta)x_0) \\
&= \delta_D(x' - |r|\sin(\theta - \gamma)), \qquad |r| = \sqrt{x_0^2 + z_0^2}, \qquad \gamma = \arctan\left(\frac{x_0}{y_0}\right)
\end{aligned}
\tag{54}
$$

17

where we in the first step use the scaling property of the delta function allowing the integral to be evaluated. Thus, we see that the Radon transform of one point is going to follow a sinusoidal path. Recognizing that an object, can be constructed as an ensemble of many points, the Radon transform of the object becomes a superposition of sine curves. Subsequently, the plot of projections $p_\theta(x')$ against the angle θ, is referred to as a sinogram [13].

Moreover, for the cases of imaging, the probed factor, is once again the projections $p_\theta(x')$. Hence the inverse form of the Radon transform is required to retrieve back the information about the original function $f(x, z)$,

$$f(x, z) = \mathcal{R}_\theta^{-1}[p_\theta(x')] \tag{55}$$

To prove the validity of this action, the Fourier slice theorem is outlined. Start with the Fourier transform of the projection $p_\theta(x')$,

$$
\begin{aligned}
\mathcal{F}p_\theta(x') &= \mathcal{F}_{x'}[\mathcal{R}_\theta f(x, z)](k_x') \\
&= \hat{p}_\theta(k_x') \\
&= \frac{1}{\sqrt{2\pi}} \int_{\mathbb{R}^3} f(x, z)\delta_D(x\cos(\theta) + z\sin(\theta) - x')e^{-ik_x'x'}\,dx\,dz\,dx' \\
&= \frac{1}{\sqrt{2\pi}} \int_{\mathbb{R}^2} f(x, z)e^{-ik_x'(x\cos(\theta)+z\sin(\theta))}\,dx\,dz
\end{aligned} \tag{56}
$$

Take the reciprocal coordinate $\boldsymbol{q} = k_x'(\cos(\theta), \sin(\theta))$ and revaluate the 2d Fourier transforms as $\mathcal{F}_r[f(x, z)](\boldsymbol{q})$,

$$\hat{p}_\theta(k_x') = \mathcal{F}_{x'}[\mathcal{R}_\theta f(x, z)](k_x') = \mathcal{F}_r[f(x, z)](\boldsymbol{q}) = \mathcal{F}_r[f(x, z)](k_x'\cos(\theta), k_x'\sin(\theta)) \tag{57}$$

which proves the invertibility of the Radon transform. In more general terms, it means that the 1d Fourier transform of the $p_\theta(x')$ is equal to 2d Fourier transform of $f(x, z)$ at a certain angle θ. Accordingly, by collecting many projections at different angles the Fourier domain of $f(x, z)$ is filled, meaning that the inverse Fourier transform, in practice retrieves the original 3d object. However, when implementing the numerical method for this algorithm one runs into a problem, namely that the Fourier domain is sampled on a rectangular grid and the projections on a polar grid. This creates significant artefacts when interpolating between the two systems. Consequently, other reconstruction algorithms are used, one of which is known as filtered back projection [14].

2.2.2 Filtered back projection

In filtered back projection the reconstruction procedure can be started by first looking at $f(x, z)$ in its inverse Fourier transform representation,

$$f(x, z) = \frac{1}{\sqrt{2\pi}} \int_{\mathbb{R}^2} \hat{f}(k_x, k_z)e^{i(k_x x + k_z z)}\,dk_x\,dk_z \tag{58}$$

form this point the rectangular coordinates is converted into polar coordinates,

$$k_x = k_x'\cos(\theta), \qquad k_z = k_x'\sin(\theta), \qquad dk_x\,dk_z = k_x'\,dk_x'\,d\theta \tag{59}$$

Thus yielding,

$$f(x,z) = \frac{1}{\sqrt{2\pi}} \int_0^{2\pi} \int_0^{\infty} \hat{f}(k'_x \cos(\theta), k'_x \sin(\theta)) e^{i(xk'_x \cos(\theta) + zk'_x \sin(\theta))} k'_x dk'_x d\theta \tag{60}$$

if the outer integral is split into $\theta = [0, \pi]$, $\theta = [\pi, 2\pi]$ and the $\theta = [\pi, 2\pi]$ is shifted by a factor π in the exponential, the following is obtained,

$$f(x,z) = \frac{1}{\sqrt{2\pi}} \int_0^{\pi} \int_0^{\infty} \hat{f}(k'_x \cos(\theta), k'_x \sin(\theta)) e^{i(xk'_x \cos(\theta) + zk'_x \sin(\theta))} k'_x dk'_x d\theta$$
$$+ \frac{1}{\sqrt{2\pi}} \int_0^{\pi} \int_0^{\infty} \hat{f}(k'_x \cos(\theta + \pi), k'_x \sin(\theta + \pi)) e^{i(xk'_x \cos(\theta + \pi) + zk'_x \sin(\theta + \pi))} k'_x dk'_x d\theta \tag{61}$$

Assuming real projection data, using the symmetry properties of the Fourier transform and taking advantage of eq. (57), eq. (61) can be written as one term,

$$f(x,z) = \frac{1}{\sqrt{2\pi}} \int_0^{\pi} \int_{-\infty}^{\infty} \hat{p}_\theta(k'_x) e^{i(xk'_x \cos(\theta) + zk'_x \sin(\theta))} |k'_x| dk'_x d\theta \tag{62}$$

Here the factor $|k'_x|$ acts as a high-pass filter to the projection, and is therefore usually identified by a filter function $\hat{h}(k'_x) = |k'_x|$. Additionally, we can rewrite the inner integral as the filtered projections Q_θ,

$$Q_\theta(x') = \frac{1}{\sqrt{2\pi}} \int_{-\infty}^{\infty} \hat{p}_\theta(k'_x) e^{ix'k'_x} |k'_x| dk'_x \tag{63}$$

and expand $x' = x\cos(\theta) + z\sin(\theta)$,

$$f(x,z) = \int_0^{\pi} Q_\theta(x\cos(\theta) + z\sin(\theta)) d\theta \tag{64}$$

Retrieving the final form of the filtered back projection [15]. To note is that our derivation was limited to a single slice in the vertical direction y'. However this is not the case for an image which is sampled on a 2d grid (x', y'), but the same method can be applied to each vertical segment as these are not coupled together for parallel beam geometries. The polar coordinate system can therefore be expanded to cylindrical coordinates, allowing the y axis to be implemented without difficulty. Meaning that for a complete projection dataset of 2d images, spanning $\theta = [0, \pi]$ the 3d volume can be constructed via the filtered back projection operator $\mathfrak{R}$ acting on the $\hat{p}_\theta(k'_x, k'_y)$ [5],

$$f(x,y,z) = \mathfrak{R}\hat{p}_\theta(k'_x, k'_y) = \frac{1}{2\pi} \int_0^{\pi} \int_{-\infty}^{\infty} \int_{-\infty}^{\infty} \hat{p}_\theta(k'_x, k'_y) e^{i(xk'_x \cos(\theta) + zk'_x \sin(\theta) + yk'_y)} |k'_x| dk'_x dk'_y d\theta \tag{65}$$

2.3 Phase retrieval

To effectively use the phase information to enhance contrast is essential when using propagation-based phase contrast imaging. There are a few ways to go about it, however, here we will limit ourselves to one of the more widely used methods derived by Paganin *et al.*[4] using a homogenous object in the transport-of-intensity framework, which subsequently gives the method its name, the homogeneous TIE phase retrieval algorithm (TIE-Hom) [5].

2.3.1 Two-dimensional phase retrieval

Start by assuming all constraints given in section 2.1.5, allowing the wave propagation to describe by the transport-of-intensity-equation eq. (39). Consider further that the imaged object can be approximated by Beer's Law eq. (34) and that the object is sufficiently thin for the phase shift to be given by eq. (32). If these two equation are substituted into eq. (39) and the exit surface at the object is said to be located at $z = 0$, it can be re-written as,

$$I(x,y,z=\Delta) = I^{in}e^{-\mu T(x,y)} - \frac{\Delta\delta}{\mu}I^{in}\nabla_\perp^2 e^{-\mu T(x,y)} = I^{in}\left(1 - \frac{\Delta\delta}{\mu}\nabla_\perp^2\right)e^{-\mu T(x,y)} \implies \quad (66)$$

$$\frac{I(x,y,z=\Delta)}{I^{in}} = \left(1 - \frac{\Delta\delta}{\mu}\nabla_\perp^2\right)e^{-\mu T(x,y)} \tag{67}$$

Now represent the exit wave image and the propagated phase contrast image as their Fourier integrals representations,

$$I^{in}e^{-\mu T(x,y)} = \frac{I^{in}}{2\pi}\iint \mathcal{F}\left(e^{-\mu T(x,y)}\right)e^{i(k_x x+k_y y)}dk_x dk_y \tag{68}$$

$$I(x,y,z=\Delta) = \frac{1}{2\pi}\iint \mathcal{F}\left(I(x,y,z=\Delta)\right)e^{i(k_x x+k_y y)}dk_x dk_y \tag{69}$$

Using the Fourier integrals representations, eq. (67) can be written as,

$$\mathcal{F}\left(e^{-\mu T(x,y)}\right) = \mu\frac{\mathcal{F}\left(I(x,y,z=\Delta)\right)}{I^{in}\left(\Delta\delta(k_x+k_y)^2+\mu\right)} \tag{70}$$

By taking the inverse Fourier transform and then the natural logarithm, the equation can be solved for the projected thickness $T(x,y)$ [4],

$$T(x,y) = -\frac{1}{\mu}\ln\left(\mathcal{F}^{-1}\left(\mu\frac{\mathcal{F}\left(I(x,y,z=\Delta)\right)}{I^{in}\left(\Delta\delta(k_x+k_y)^2+\mu\right)}\right)\right) \tag{71}$$

2.3.2 Three-dimensional phase retrieval

To extend the phase retrieval to three dimensions, we need to recall section 2.2, as the filtered back projection algorithm is essential. Attention can now be directed towards the problem at hand, namely trying to extract the filtering step from the two-dimensional projections, into the reconstructed 3d volume [5].

Hence the first step is to linearize the exponential coming from Beer's law of transmission eq. (34) and connecting it to the projection of the object,

$$e^{-\mu T(x',y)} \approx 1 - \mu T(x',y) = 1 - \mu p_\theta(x',y) \tag{72}$$

If we further assume that the object is composed of a single light element, then a proportionality constant $\alpha = \delta/\beta$ could be introduced and would hold for the complex refractive index of the material. A reasonable assumption, given our material restriction is currently

to uphold the projection approximation. To that end when can apply this assumption and rearrange eq. (67),

$$1 - \frac{I(x', y', z' = \Delta)}{I^{in}} = \left(\frac{2k}{\alpha} - \Delta \nabla_\perp^2 \right) p_\theta(x', y) \tag{73}$$

Now the projection approximation is reasserted with emphasis on the constraint of weak phase contrast, which the approximation enforces. Implicitly this has been done before within the TIE derivation, but not explicitly expressed. Then use the in-line contrast function $K(x', y', z')$, as introduced by D.A. Thompson *et al.* [5], to express the intensity terms, and then approximate the function with a first-order Taylor expansion,

$$\boldsymbol{K(x', y', z')} = -\ln\left(\frac{\boldsymbol{I(x', y', z' = \Delta)}}{\boldsymbol{I^{in}}} \right) \approx 1 - \frac{\boldsymbol{I(x', y', z' = \Delta)}}{\boldsymbol{I^{in}}} \tag{74}$$

Taking the Fourier transform of eq. (73), we again obtain the 2d phase retrieval step from before eq. (70),

$$\mathcal{F}p_\theta(x', y) = \frac{\mathcal{F}(K(x', y'))}{\frac{2k}{\alpha} + \Delta(k_x + k_y)^2} \tag{75}$$

Here the left hand side can be identified in the same way as in eq. (57) giving,

$$\hat{p}_\theta(k_x', k_y') = \frac{\mathcal{F}(K(x', y'))}{\frac{2k}{\alpha} + \Delta(k_x + k_y)^2} \tag{76}$$

From this point the filtered back projection operator $\mathfrak{R}$ can be applied to both sides,

$$\mathfrak{R}\hat{p}_\theta(k_x', k_y') = \mathfrak{R}\left[\frac{\mathcal{F}(K(x', y'))}{\frac{2k}{\alpha} + \Delta(k_x + k_y)^2} \right] = f(x, y, z) \tag{77}$$

Note that the Laplacian in eq. (73) was evaluate by the Fourier space Laplacian identity. However if the $\left(\frac{2k}{\alpha} - \Delta \nabla^2 \right)$ factor is directly applied to eq. (77),

$$\left(\frac{2k}{\alpha} - \Delta \nabla^2 \right) f(x, y, z) = \left(\frac{2k}{\alpha} - \Delta \nabla^2 \right) \mathfrak{R}\left[\frac{\mathcal{F}(K(x', y'))}{\frac{2k}{\alpha} + \Delta(k_x + k_y)^2} \right] \tag{78}$$

Evaluating the right hand side by first taking the Laplacian of the explicit form of $\mathfrak{R}$,

$$\nabla^2 e^{i(xk_x' \cos(\theta) + zk_x' \sin(\theta) + yk_y')} = -(k_x + k_y)^2 e^{i(xk_x' \cos(\theta) + zk_x' \sin(\theta) + yk_y')} \tag{79}$$

the denominator factor cancels out,

$$\mathfrak{R}\left[\frac{\left(\frac{2k}{\alpha} + \Delta(k_x + k_y)^2 \right) \mathcal{F}(K(x', y'))}{\frac{2k}{\alpha} + \Delta(k_x + k_y)^2} \right] = \mathfrak{R}\left[\mathcal{F}(K(x', y')) \right] \tag{80}$$

Inverting the left hand side of eq. (78) concludes the derivation, showing the validity of phase retrieval in the reconstructed 3d volume [5].

$$f(x, y, z) = \left(\frac{2k}{\alpha} - \Delta \nabla^2 \right)^{-1} \mathfrak{R}\left[\mathcal{F}(K(x', y')) \right] \tag{81}$$
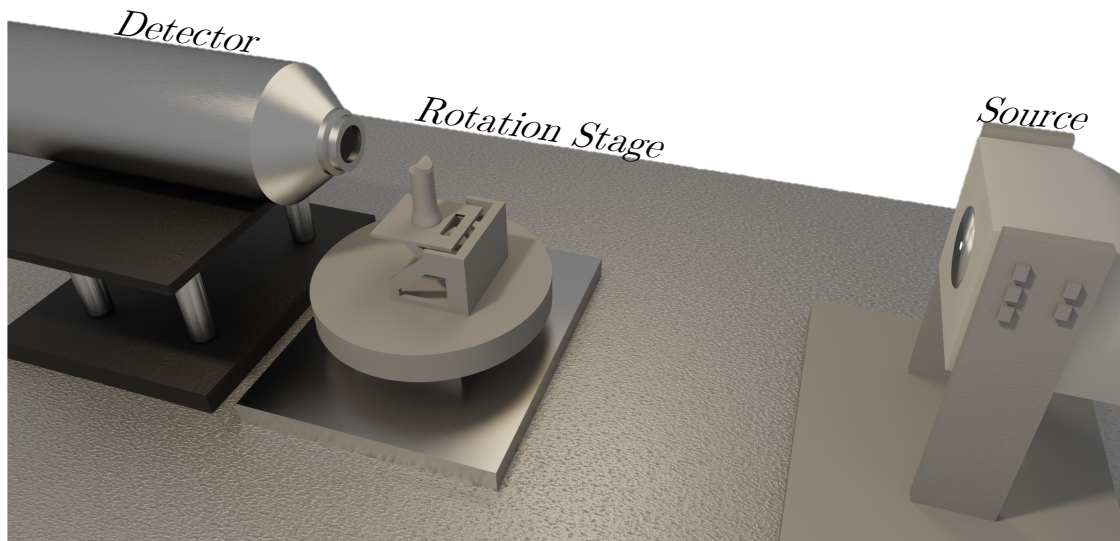
3 Method

3.1 Laboratory equipment

Figure 8: Overview of the main components contributing to the propagation-based phase-contrast imaging. Starting from the right is the source, a microfocus X-ray tube with a copper target, producing X-rays by bremsstrahlung and X-ray fluorescence. Next is the rotation stage, which is comprised of three different interlinked components. The first level is a step motor allowing for motion along the optical axis and in the horizontal direction. On top of that is the rotation motor and finally a high precision step motor. This one can move along all axes allowing the user to align the rotation centre of the sample. The last main component is the detector, it uses a scintillator-based lens-coupled CCD to capture the X-rays and convert them into an electrical signal.

3.1.1 X-ray source

Since the discovery of X-rays in 1895 by Wilhelm Röntgen, X-ray tubes have been used as the primary source for X-rays. Yet, during the 1980s, dedicated synchrotron radiation facility overtook them as the primary means of production for X-ray research, as they provide higher photon flux coupled with higher coherence. As a result, X-ray tubes saw less use in areas where a high resolution was necessary.

However, with the development of microfocus X-ray tubes, the micrometre regime was available to lab-based set-ups. Hence these experimental stations opened up the possibility for much smaller modular systems as seen in fig. 8, where nanometer resolution was not necessary, and this is where they come in for propagation-based phase-contrast tomography. In many cases, tomography would benefit from higher resolution, but if the sample in question has interesting features on the micrometre scale, doing a measurement on the more available lab-based system could save time and resources.

There are a few available types of microfocus X-ray tubes, but most commonly, X-rays are produced via acceleration of electrons onto a metal anode target resulting in two effects. The first is a deceleration of the electrons, which subsequently gives a continuous broad spectrum of radiation known as bremsstrahlung or braking radiation. The second effect is fluorescent

radiation, which occurs when an electron knocks out an electron in an inner shell, such that an electron vacancy can be created. Once an outer shell electron undergoes relaxation, it fills the inner shell vacancy, which can result in the emission of a characteristic X-ray photon. Its energy will be that of the difference between the two states. As a result, these lines are highly monochromatic compared to the bremsstrahlung [10]. The characteristic line transitions are usually denoted in Siegbahn notation.

For X-ray tubes, the most pronounced peaks are that of the K_α and K_β, which are due to the transition of either an L shell or M shell electron to the K shell respectively. These are commonly further split into K_{α_1}, K_{α_2} and K_{β_1}, K_{β_3} which denotes the spin-orbit state of the electron. These spin-orbit states can usually not be distinguished, and hence the transition is only denoted by the primary line. The spectrum produced by our specific model, a microfocus copper X-ray tube, can be seen in fig. 9.
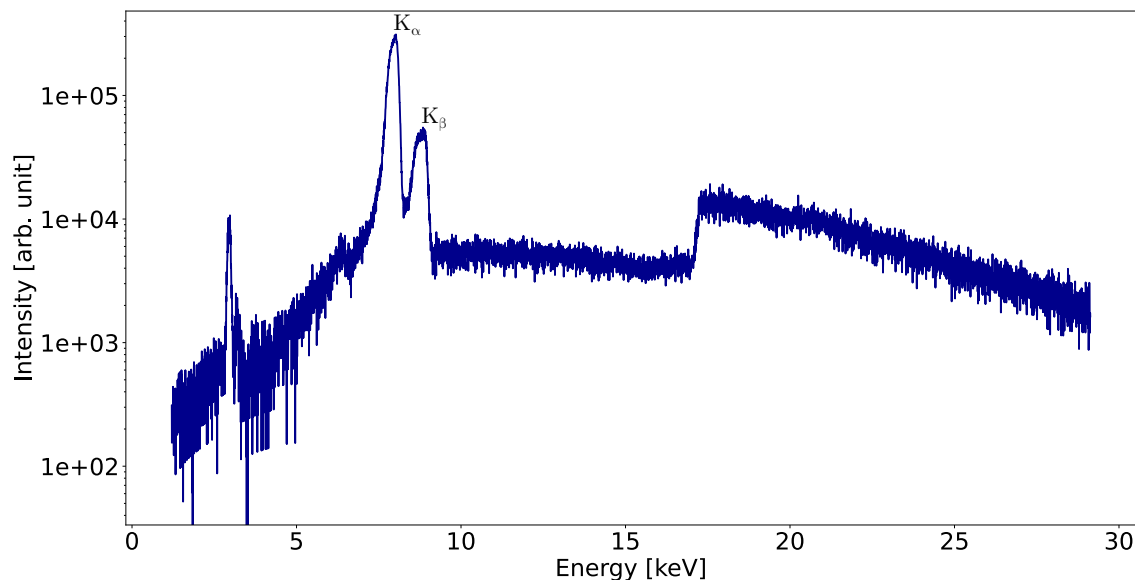
Figure 9: Logarithmic intensities for the Bremsstrahlung spectrum with the characteristics fluorescent radiation lines K_α, K_β superimposed. The spectrum was produced by the laboratory Cu X-ray tube.

The produced radiation coming from the metal target is approximately isotropic. Therefore, to increase the effectiveness, the electron beam is magnetically focused onto a small spot on the target, as in fig. 10. Unfortunately, this results in the drawback that the target gets extremely hot, as only 1% of the energy coming from the electron beam gets converted into X-rays. Hence the system needs to be cooled, and for a stationary target, this means an external cooling system, usually a water cooling loop [11].

This increased heat further limits the choice of material to ones that can withstand high heat and have good thermal conductivity. Due to the heat limitations for a small electron beam spot the overall operational power of the system is constrained, lowering the flux and resulting in overall longer measurement times. The benefit is that the coherence of the beam is increased, allowing for higher resolution measurements. Finally, the specific model of X-ray tube used at the laboratory is, as mentioned before, a microfocus Cu X-ray tube from Rigaku, with a nominal spot size of 25 μm (FWHM 45 kV).
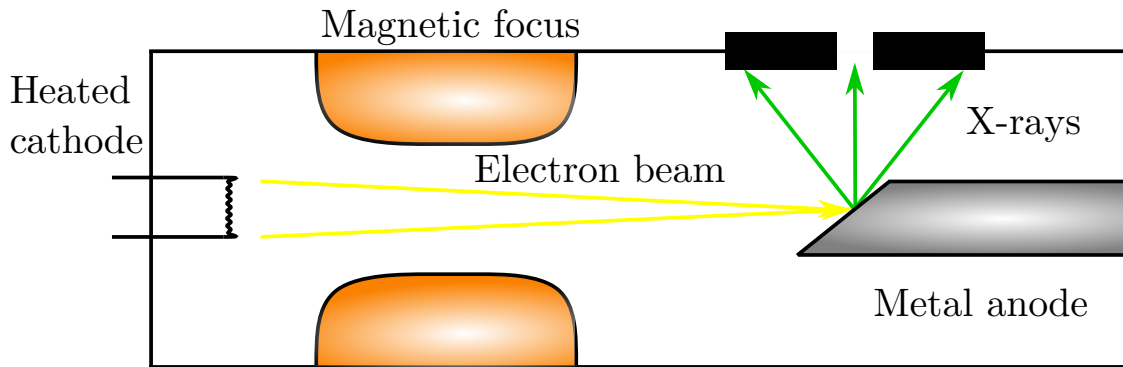
23

Figure 10: Simplified schematic of the main components inside a microfocus X-ray tube. The electrons are generated by exerting a high negative voltage on a heating cathode. Once created, the electrons accelerate towards the positive metal anode. On the way to the target, the electron beam is magnetically focused onto a smaller region of the target, which subsequently produces X-rays. These rays are still divergent, hence only a small selection of the X-rays can pass through the beam spot.

3.1.2 Scintillator based detector

X-rays detectors based on direct illumination, such as photon-counting detectors have limited resolution, since the pixel size generally ranges between tens and hundreds of microns. However, by indirectly detecting the X-rays with a scintillator screen, the radiation can first be absorbed and converted into visible light. The light can subsequently be detected by a CCD or a complementary metal-oxide-semiconductor (CMOS).

This additional step allows the light to be focused using regular optics, such as a focusing lens or a fibre-optic plate. As a result, the effective resolution of an indirect detection system can be much higher than for a direct detector. The main caveat is that these detectors are inefficient due to the scintillation and smaller pixel size, which together leads to longer exposure times [13]. Our setup uses a scintillator-based lens-coupled CCD with an effective pixel size of 0.55 µm, from Rigaku XSight (lens unit LC 0540), see fig. 9.

3.1.3 Rotation stage

So far, we have given an overview of the source and detector, but we have yet to mention one of the most important pieces of equipment for tomography, namely the rotation stage. It needs to be highly precise, since any drift or instabilities in the sampling of the projections will cause the Radon transform to be incorrectly sampled, resulting in artefacts in the reconstructed volume. Later sections will identify and try to numerical solve some of these issues, but a precise rotation stage severely alleviates these problems.

One problem that can happen with the rotation stage is that it is not perfectly aligned. In that case, the misalignment gives rise to two possible tilting angles, the pitch angle ν and the roll angle ζ, as seen in fig. 11. The pitch angle ν results in a translation along the z axis, which in turn causes a shift along the tomographic axis y. A misaligned pitch angled can be corrected by tilting the detector by the same amount such that the effect cancels out. The pitch angle can then be calculated as,

$$\nu = \arctan \frac{\Delta y}{\Delta z} \tag{82}$$

where, Δy is the shift along the vertical direction, and Δz is the horizontal shift.

As for the roll angle ζ it can readily be corrected by pre-processing procedure where each projection is tilted in accord with,

$$\zeta = \arctan \frac{\Delta x}{\Delta y} \tag{83}$$

where, Δy again is the shift along the vertical direction, and Δx is the horizontal shift [13].
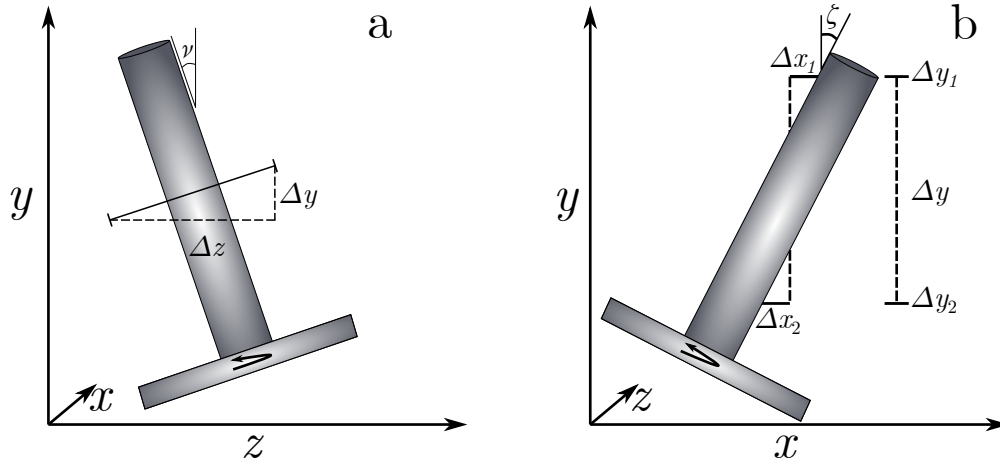

Figure 11: Schematic of the two misalignment angels in the rotations stage. The beam direction is z and the correct tomographic axis is y, with (a) depicting the pitch angle ν which causes a translation along the z axis, resulting in a shift along the tomographic axis y. This effect is solved by correctly aligning the detector. In the right figure (b), the roll angle ζ can be seen. This also causes a shift along the tomographic axis, but it can readily be fixed in pre-processing [13].

3.2 Tomographic artefacts

Artefacts in tomography are a frequent occurrence for most lab-based step-ups. As such, knowledge of where these issues come from and how to potentially resolve them or limit their effect is of great importance. This section will describe four of the more common artefacts, their origins and how they can be resolved.

For reconstruction algorithms such as the filtered back projection, a common assumption is that the sample is rotated around the vertical centre line of the detector plane. However, this is not true in most cases, and the result of this misalignment is that the reconstruction algorithms incorrectly correlate the projections information leading to artefacts as can be seen in fig. 12 (b). However, if the object is always contained within the field of view, the correct position of the rotation axis can be found unless other defects are present.

There is also a possibility for a misaligned roll angle ζ, see section 3.1.3. The problem then is that each rotation angle is slightly tilted, leading to a linear difference in the rotation centre for the top and bottom feature. To fix this each projection can be tilted in accord with eq. (83) [13].
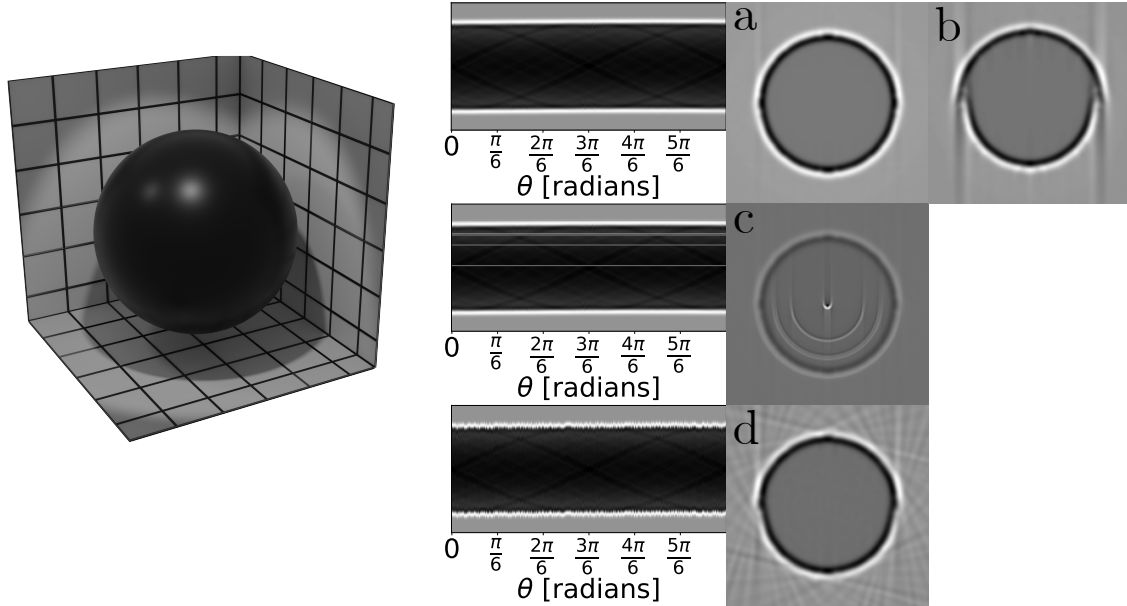
Figure 12: Illustration of three different tomographic artefacts for a spherical object. In figure (a) the object has been reconstructed with the correct rotation centre while in (b) the rotation centre has been assigned slightly off-centre. This results in the reconstruction not correctly closing. In (c) a few detector pixels have been randomly selected to be unresponsive, which results in the common stripe defects inside of the sinogram and ring artefacts in the reconstruction. Finally, in (d), each projection has been randomly shift in the horizontal direction by small amount, indicative of a unstable rotation stage. The resulting reconstruction is not severely disturbed as the motion is much smaller than the size of the object.

Another common tomographic artefact is ring artefacts. These artefacts are due to faulty pixel values, and as such, are stationary throughout the acquisition. Hence they appear as rings in reconstructions. However, due to the sampling rate of $\theta = [0, \pi]$, these artefacts instead appears as half-rings as seen by fig. 12 (c). Ring artefacts can reliably be resolved by numerical algorithms that target their stationary nature, In this thesis, two approaches have been used and will be described in section 3.4.

There can also be a problem with the stability of the sample, which can either be an unstable rotation stage or the effect of something external. The result is a motion artefact. These artefacts are among the most difficult ones to solve as they can have many forms and destroy the assumption of a stationary geometry. In the case of randomized horizontal motion, as in fig. 12 (d), it can be hard to resolve the correct object unless there is some symmetry to exploit. There are a few methods that have been able to resolve the issue but at the cost of high computational times [16]. If the motion is linear and the object is contained within the field of view (FoV) for all projection, then each projection can simply be shifted by the same amount as it has moved.

For large vertical motion, the tomography reconstruction will be meaningless, since the back projection of each line will now be associated with the incorrect attenuation [17]. But if the motion is sufficiently small, a well-defined feature can be tracked throughout the projections, and the motion recorded, allowing for a motion-correction. Another possibility is that the rotation stage has run-out errors, but this motion is difficult to measure without specialised equipment that precisely track the sample rotation [18].

3.3 Experimental operation

Due to the modular nature of the used lab-based system, there is always a need for a new alignment when operating at a new geometry fig. 8. The first step is to align of the detector to the optical axis. This is done via the use of a circular centring jig. The shadow image of the pinhole will show deviations from a circular shape when the detector is shifted or tilted to the optical axis. The alignment includes shifting the detector along the horizontal direction and the source vertically with a manual micrometer-step stage until the pinhole appears circular.

Assume that an already prepared sampled is placed on the rotation stage. The first procedure is then to align the rotation centre. This can be achieved by first moving the sample into the FoV using the lower linear motors and collecting a projection. The object is then rotated by 180°, and another image is acquired. If the object moves outside of the FoV, the upper horizontal motor x is moved, and the object is rotated back to 0°. This process continues until the rotation is stable. The same procured is the repeated, but for the z direction by viewing the 90° to 270° rotation.

Once the rotation centre has been aligned, the object is moved out of the FoV to allow for the collection of the background images. This background is divided into two parts. The first one is dark fields, which refers to the background intensity caused by electrical fluctuations and cosmic particles. The second part is the bright field, referring to the detector being illuminated by the source beam. Together these are referred to as flat fields. Furthermore, by applying flat field corrections to the projections, they can be normalized and corrected for the fixed-pattern noise. Additionally, the flat fields are always collected in pairs of 10 to decrease the effect of hot pixels and use the same exposure time as the subsequent projection acquisition.

With the first set of flat fields collected, an appropriate exposure time and angles step size is selected, and tomographic measurement starts. Furthermore, as the detector response sometimes changes through time, due to saturation, a second set of flat fields are collect directly after the projection acquisition, concluding the experimental operation. The next step will deal with the pre-processing of the acquired data.

3.4 Preprocessing

Artefacts are an ever-present problem in tomographic imaging. Luckily algorithms have been developed which effectively minimize or even removes some of the artefacts from section 3.2. In thesis work has been done in developing new ways and implementing exiting ones into a coherent python pipeline. Most of the new functions has been personally devolved, except for the 3d phase retrieval and the locating of unresponsive pixel fig. 13, which has undergone iterative development with supervision.

Correcting for a misaligned rotation axis can either be straight forward or very hard, depending on the severity of the problem. So start by assuming that the object is in the FoV throughout the acquisition. The issue can then be that the object is not rotating around the exact centre of the horizontal detector length n_x. To find the correct rotation centre a feature located at x_1, y_1 in the first projection where the angle is 0° is selected. The same feature is then selected from the horizontally flipped last projection at angle 180° now located at

x_2, y_2. The length Δ between the two positions can then be calculated,

$$\Delta = \frac{x_1 + x_2}{2} - \frac{n_x}{2} \tag{84}$$

from which the correct rotation centre can be found.

```
┌─────────────────────────────────┐   ┌──────────────────────────────────────────────────┐
│ 1. Load flat-field images.      │   │ 1. Apply the stripe removal algorithm from TomoPy. │
│ 2. Locate unresponsive pixels.  │   │ 2. Set undefined pixel values to 1.                │
│ 3. Calculate the mean flat-field.│──▶│ 3. Set a lower intensity value limit of 0.0001.   │
│ 4. Apply flat-field corrections │   │ 4. Normalize the outer corners of each projection to 1. │
│    and blur unresponsive pixels.│   │ 5. Apply -ln(I) or (1-I) to the projections.      │
└─────────────────────────────────┘   │ 6. Rotate each projection by the roll angle.      │
                                       └──────────────────────────────────────────────────┘
```

This depends on how the in-line contrast function is approximated.

```
        ┌────────────────────────┐         ┌──────────────────────────────────┐
        │ 1. Locate the rotation │────────▶│ 1.Reconstruct the object using   │
        │    centre.             │         │ Tomopy's filtered back projection │
        └────────────────────────┘         │ algorithm with a cosine frequency filter. │
                                           └──────────────────────────────────┘
┌──────────────────────────────────┐              │
│ 1. Apply the 2D phase retrieval. │         ┌──────────────────────────────────┐
└──────────────────────────────────┘         │ 1. Apply the 3D phase retrieval. │
                                             └──────────────────────────────────┘
┌──────────────────────────────────┐
│ 1.Reconstruct the object using   │
│ Tomopy's filtered back projection │
│ algorithm with a cosine frequency filter. │
└──────────────────────────────────┘
```
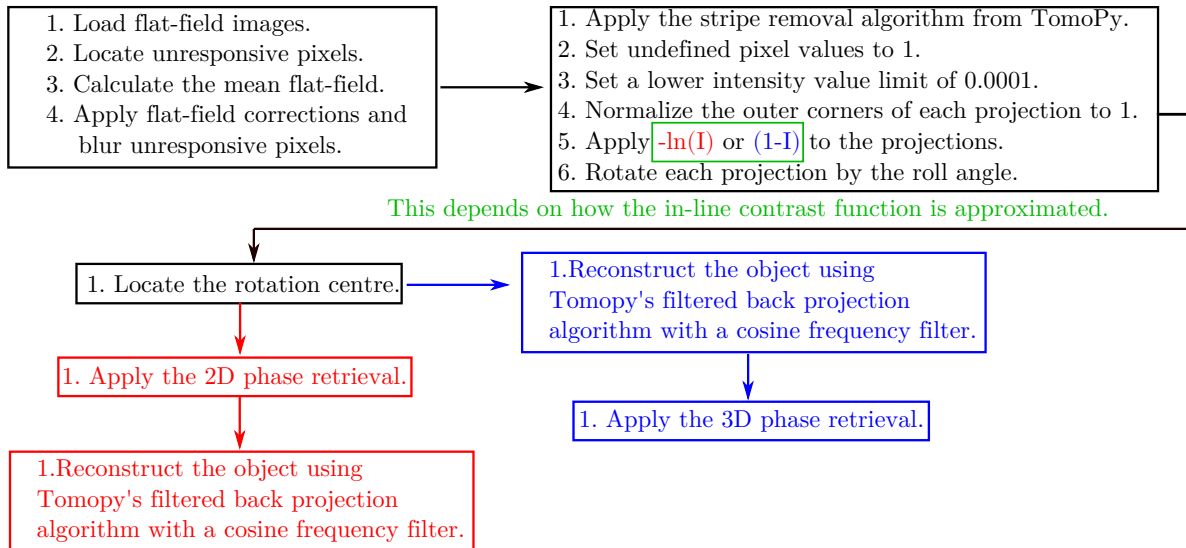
Figure 13: Flowchart of standard preprocessing procedure. Assumes that the roll angle has already been found. If this is not the case skip step 6 in box two and instead do it as step 2 in box three.

Furthermore, there might be a problem with the rotation stage roll angle ζ, see fig. 11. This problem can be fixed after the rotation centre has been found, as there will still be a slight deviation in accord with eq. (83). By calculating the roll angle and rotating each projection by the found angle, the tilt artefact can be resolved [13]. To note here is this tilt should always be the last thing that is corrected, as it could otherwise introduce problems for the other algorithms. Furthermore, the roll angle rarely moves, so once it has been found for the system, there is usually little need to adjusted the value.

Ring artefacts are another commonly encountered problem, and we opted to use two methods to limit their effect on the image quality. The first method was developed in-house and it probed the dark and bright-field images for inconsistency still remaining in the detector response, meaning that the location of unresponsive pixels could be recorded and then corrected for when doing the flat field corrections. Even so, this approach did not deal with all ring artefacts. Therefore, the second used algorithm was the three-step method developed by Vo *et al.* [19]. This algorithm is part of TomoPy, a widely used python package for tomographic data processing and image reconstruction and has many useful features for dealing with these types of problems. The algorithm works by finding and targeting small, medium and large stripe artefacts individually in the sinograms, and consequently blurring them, which eliminates most of the present defects.

After ring removal, undefined pixel values are set to 1, which represent a pixel value of no absorption. A lower intensity bound is also asserted to 0.0001 to not run into potential problems if the in-line contrast function is evaluated as the negative natural logarithm.

Assuming that the rotation centre has already found, the method now splits into two paths. One path dealing with phase retrieval in the projections, and another where the phase corrections are done in the reconstructed volume.

In both cases, the reconstruction step is done via filtered back projection section 2.2.2. The numerical implementation of this algorithm is provided by TomoPy, as is the 2d TIE phase retrieval step. For the sake of clarity, we note that TomoPy uses what they call the regularization parameter as an input variable, this is simply the inverse of the proportionality constant. Additionally, the numerical implementation of 3d TIE phase retrieval has been done internally by extending the TomoPy function with an additional dimension.

3.5 Numerical modelling

Create Phantom ⟶ Polychromatic corrections ⟶ Apply cylindrical mask ⟶ Multiply the phantom with each effective value creating two 3d arrays

1. Project each array around the centre of the volume for $\theta = [0, \pi]$

For each projection,
1. Upscale image by a factor of 2
2. Calculate transmission and use the Fresnel filter
3. Take the modulus square of the result
4. Apply the OTF of the system
5. Interpolate to the detector plane

Figure 14: Flowchart of the main elements inside of the numerical model.

The numerical modelling of phase propagation for this thesis is based on the work by Ulf Lundström, where the numerical model was used for angiography, the imaging of blood vessels [11]. However, to make this method viable for our specific needs, a few extension were made. One of these extensions was the creation of a phantom object. This phantom gave us more information when evaluating the final reconstruction, as the phantom could be used as ground truth for the simulated object. We opted to create a complete 3d volume through a python package, know as TomoPhantom [20].

Given that the simulations should be as close as possible to our experimental parameters, they had to properly deal with the broadband radiation coming from the source. It can be sufficient to approximate the radiation by selecting the characteristics line produced by the bremsstrahlung. However, this can lead to an incorrect depiction of the phase contrast. Hence a better approximation is to deal with the polychromatic case and do a complete integration of the energy dependant terms (E, λ, k). Yet, this is, in most cases, quite difficult, so another way of obtaining a similar result is to do a weighted average of the bremsstrahlung spectrum and the detector response for each energy. In this way an effective wavelength λ_{eff} for the setup can be calculated [12].

In the same way, as with the wavelength, the atomic scattering factors were evaluated. The user only needs to specify what atomic composition and mass density the material has. These variables then allow the determination of the effective linear attenuation coefficient μ_{eff} and effective phase shift ϕ_{eff}. Before μ_{eff}, ϕ_{eff} are inserted the phantom is prepared for projecting by applying a cylindrical mask around the tomographic axis. Doing this ensures that the object always is within the simulated FoV.

The phantom now contains two 3d objects, one with the effective linear attenuation coefficient of each pixel and another with the effective phase shift. To form the tomographic dataset each volume had to be projected onto a 2d plane. This was done by taking each pixel and integrating it in the direction of optical axis. The object was then rotated by a specified angle around a set rotation centre, upon which the object was projected on to the 2d plane again. By doing this for a linear step of angles going from $0° \rightarrow 180°$ two projection dataset were created.

This concludes the extensions to the numerical model, and the next steps will handle the propagation of the individual projections. To start, a few variables are needed, namely the size of each pixel in the 3d phantom, the detector pixel size, the source to detector distance z_{tot} and the object to detector distance z_2. These values define the simulation planes, the magnification and effective propagation distance z_{eff}. Additionally, if the optical transfer function of the system is to be included, see section 2.1.7, one needs to assign the standard deviation of intensity PSF due to the detector $\sigma_{detector}$ and the source σ_{source}.

In order to calculate the Fresnel propagator the first step is to create the Fourier grid, upon which the simulation takes places. This is done by upsampling each projection by a factor of two, such that the higher frequency terms are accurately represented. Additionally the Cartesian grid defining the detector plane is calculated using the detector pixel size scaled by the magnification.

When both grids have been created, the upsampled projections are used for the propagation. First the transmission function is calculated in according with the projection approximation eq. (30). The transmission is then propagated via convolution with the Fresnel propagator eq. (15) in the Fourier domain. The intensity of the exit wave is then acquired by inverse Fourier transforming the result and taking the modulus squared.

The next step is to blur the image with the MTF of the detector, an area pixel and the source. Here we assume that both detector and source have a Gaussian profile. For the pixels, an area integration is done as this help with interpolating the simulation plane values on to the detector plane.

The intensity image now represent the one obtained from eq. (51). However, as we want the final image to be representative of a real measurement the image is finally interpolated onto the detector grid. This procedure is done for all projections. Once the whole tomographic dataset has been propagated, either the 2d projections are phase-retrieved and then the volume is reconstructed or the volume is directly reconstructed and then phase retrieved in 3d.

4 Results

Phase retrieval based on the TIE framework is one of the most commonly used methods to retrieve the projected object thickness for propagation-based X-ray phase-contrast tomography. In this framework two algorithms exists, one based on retrieval in the projections (see section 2.3.1) and another in the reconstructed volume (see section 2.3.2). The 3d phase retrieval has been shown to increase noise suppression while reducing overall computational times [5]. However, this approach assumes a linear in-line contrast function which require the object to uphold weak phase contrast.

In the first section, we aim to test this approximation and compare both phase retrieval approaches on a phantom composed of rectangular cuboids features. This phantom shape exaggerates the potential shortcomings for objects features with long, straight and aligned features, which should exhibit rapidly changing integrated thickness while rotated, and increased edge phase contrast. The second section deals with similar feature types in a laboratory setting, with a wood splinter as a sample. The final section aims to bridge the information gap between the laboratory measurement and the first simulation, by using a segmented version of a wood splinter as a phantom for the simulation.

4.1 Simulations with overlapping rectangular cuboids

4.1.1 Validity of a weakly absorbing object
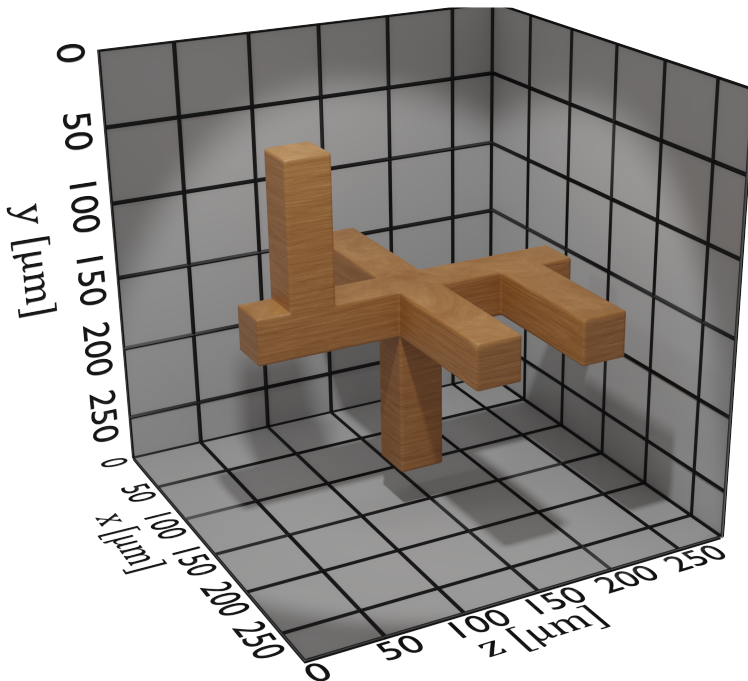
Figure 15: A illustrative overview of the created phantom.

Propagation-based X-ray phase-contrast imaging relies on the validity of a weakly absorbing object with a weak phase contrast. However, lab-based samples can potentially reach object

31

sizes where the absorption or phase contrast is too high, restricting the use of an approximated in-line contrast function eq. (74). As a result, the phase retrieval operator on the 3d reconstructed object would not be valid, motivating a closer evaluation.

To test this hypothesis, we will first look at the discrepancy in the in-line contrast function for unfavourable objects geometries, particularly where long straight feature are perpendicular to the tomographic axis. Large deviations would imply that phase retrieval in the reconstructed 3d volume is not valid.

We therefore created a phantom object that contains two distinct groups of side planes, see fig. 15. These groups are straight sections with an surface normal either parallel to perpendicular to the tomographic axis. Additionally, the object is assumed to be composed of only a single material, that being C_5O_6H with a density of 700 kg/m^3. Here, the chemical properties were disregarded and the material was selected to have a comparable composition to wood [21]. The phantom pixel size was set to be 0.55 µm and the whole matrix was 512 pixels in all directions. This is relatively small compared to lab-based objects, which are usually about 2 to 3 times larger. However, wood is rarely perfectly straight and contains tubular structures filled with air when dry, making the width of the phantom closer to the total integrated thickness of such an object.

The simulated distances were selected in accordance to real distances used during a measurement, which have been found to be optimal for the targeted experimental station [12]. As such, the total distance z_{tot} was set to 9.9 cm, with the sample to detector distance z_2 being 0.9 cm, which assures a preferable magnification of $M = 1.1$.
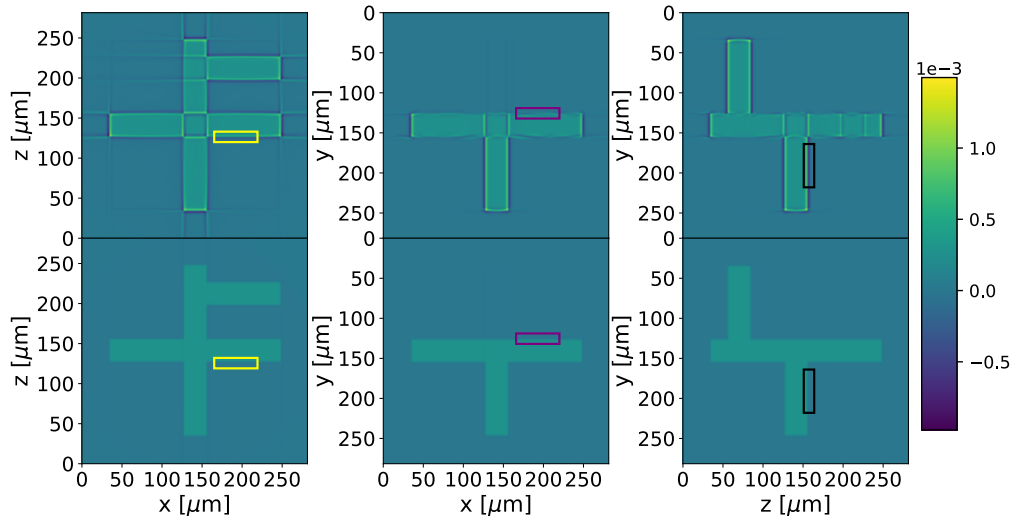

Figure 16: In the top section is a reconstruction of the simulation with propagation distance of $z_2 = 0.9$ cm, resulting in the formation of distinct phase fringes. The intensity has further be assumed to follow the none approximated version of the in-line contrast function. The bottom section shows the same cut-outs but for an object in the contact region $z_2 = 0$ which only shows the absorption contrast, again with the intensity as $-\ln(I)$. The three different region of interest (ROIs) shows areas that will be further investigated. This as they all show very different phase fringe formation.

Simulating the propagation via the method described before, in section 3.5, using the aforementioned parameters, a set of 400 equidistant projections between $\theta = [0, \pi]$ was obtained. In addition, another simulation in the contact regime (z_2=0) was also performed. The con-

tact regime was used to provide a control set which only deals with the intensity due to Beer-Lambert's law of absorption eq. (34), and as such acts as a reference for the absorption contrast.

After creating both datasets we choose to test the validity of the in-line contrast function eq. (74) by seeing how the Taylor expansion holds when it is used for the reconstruction. The analysis was only done on three different limited regions, denoted by yellow, purple and black in fig. 16. Note that there are some peculiar features on this object in particular the phase fringes. However, in this section we will primarily deal with the validity of approximating the in-line contrast function, leaving the review of the fringes shape to section 4.1.2.
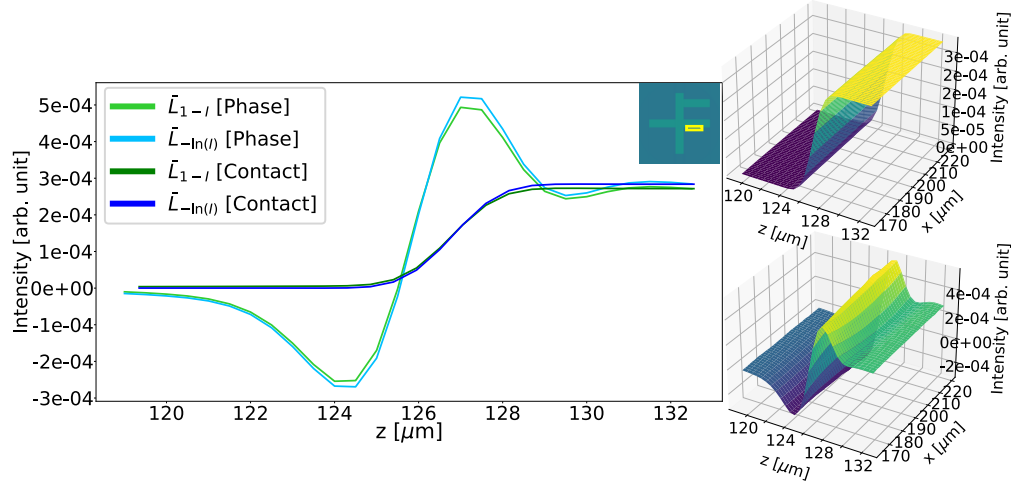
Figure 17: Closer inspection of the yellow ROI edge profiles. The main plot shows the average line profile for the different simulations, with (lightgreen) showing the phase fringe with the in-line contrast function approximated while the (lightblue) one has remained untouched. The same is true for the contact region where the (darkgreen) displays the edge when the intensity approximated and (darkblue) not. Next to the average line profiles are the surface plots of the phase fringe and contact edge with intensity set as $-\ln(I)$.

In fig. 17 the fringe/edge is averaged along the x-direction and the absolute difference between the reconstruction with and without approximated intensity is taken. To get a value that is more easily comparable when using different simulation parameters, the absolute difference is also normalized with the maximum value of the averaged none approximated $\bar{L}_{-\ln(I)}$ fringe.

$$AD = \frac{\left| \bar{L}_{-\ln(I)} - \bar{L}_{1-I} \right|}{\max\left(\bar{L}_{-\ln(I)} \right)} \tag{85}$$

To obtain a single value representing the discrepancy between the two reconstructions the mean of the normalized absolute difference $\bar{AD}$ is taken. From this point the same simulation is repeated with different mass densities to see where the approximation starts to affect the reconstruction.

In fig. 18, the difference is higher for the phase fringe than for the contact region. This increased difference for the phase fringe is quite natural given that the maximum and minimum intensities are higher, resulting in it being more affected by the approximation. The results show that the dependence of the phase fringe difference on the mass density is not logarithmic. It especially appears to deviate for mass density over 100 kg/m^3.

33

Looking at the black region of interest, one might expect the approximation to perform poorly, as the intensity is higher. Yet, this not the case since the approximation is applied on each projection, and the integrated thickness of this section is small, resulting in a good agreement of eq. (74).
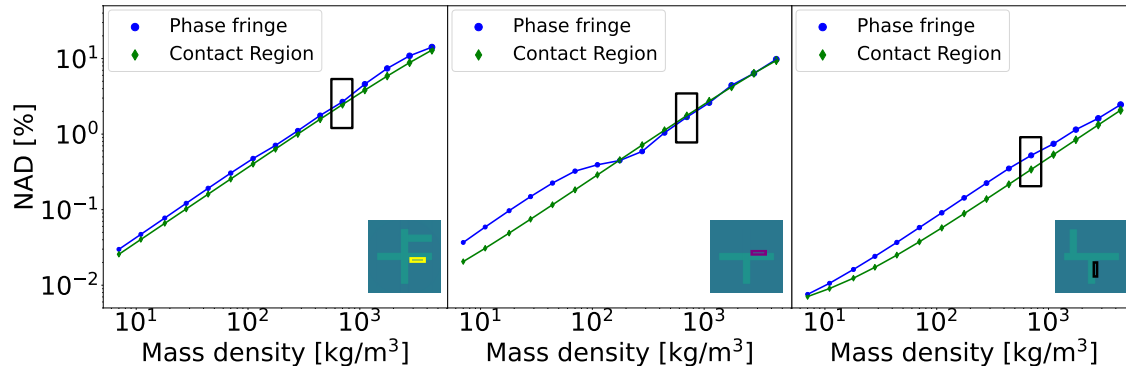

Figure 18: The normalized absolute difference when the in-line contrast has been given by $-\ln(I)$ and $1-I$ for a logarithmic range of densities. The blue features depict the difference in the phase fringe, while the green shows the difference in the contact region. The black rectangle indicates the reference value of 700 kg/m^3. Each plot shows the difference in a local area, as indicated by the coloured ROI on the reconstructed slice.

The higher intensity seen in the reconstruction can qualitatively be understood when viewing the sinogram in this region, fig. 19. Here the sinogram displays a smooth and stable nature, such that when viewing the reconstruction step eq. (65) the line integrals will retrieve an object with well-defined edges.

Applying the same line of reasoning for a sinogram located within the yellow region, we see that the consistency between different angles is not optimal. Especially with angular views close to where the object is parallel with the optical axis 90°, as this angular region will have an object that is rapidly changing in integrated thickness due to the shape of the phantom.
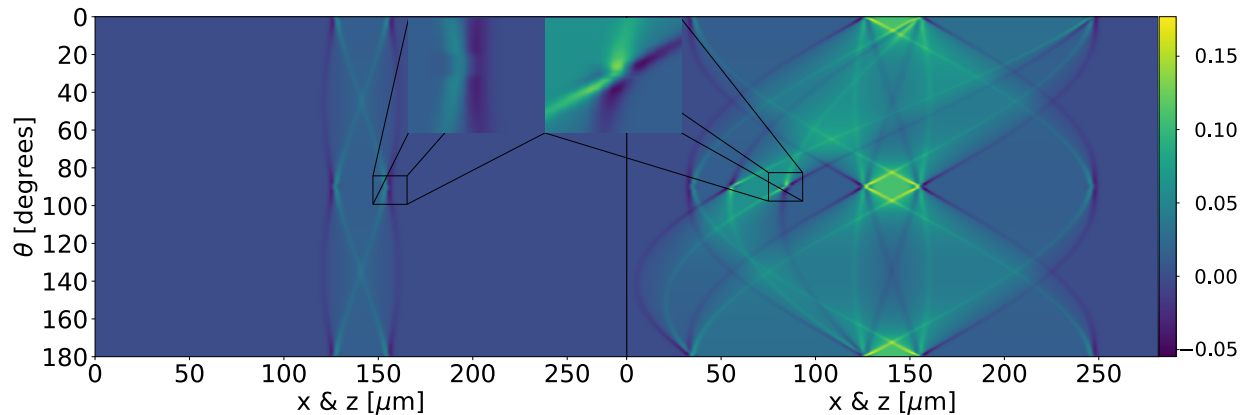

Figure 19: Sinograms for the straight-edged phantom with a mass density of 700 kg/m^3. The left image shows the sinogram at y = 200 μm which show a smooth intensity curve. The second sinogram to the right is taken at y = 140 μm and for which sharp intensity fluctuations occurs at around 90° when the object is parallel to the beam.

34

This argument of consistency in the sinogram due to a rapidly changing integrated thickness have previously been encountered within the contact region. The defect was then attributed to the exponential edge-gradient effect [6], a non-linear error resulting from the exponential integration of different intensity components. The effect is found for long and highly absorbing features, as the relative change from one projection to another can be very large.

However, if the difference was to be correlated with the exponential edge-gradient effect, the reconstruction within the contact region should exhibit deviations from the logarithmic path for higher mass densities. This is not the case given the low absorbing nature of the object. As a result, the higher degree of inconsistency in the sinogram for the propagate object could be due to the phase interference increasing the feature contrast and subsequently enlarging the discrepancy, allowing for this defect to appear for low absorbing features.

Even so, the small deviations from the contact region for the phase fringes reinforce the current consensus, namely that the in-line contrast function can be approximated with a first-order Taylor expansion, if the material is low absorbing. However, there will be a slight difference in the contrast, which could affect the result.

The next section will focus on the deteriorating effects on the fringe structure due to the sharp edges of the object. Also, the Taylor expansion of the in-line contrast function will henceforth always be applied, unless stated otherwise, as the approximation is essential for the derivation of 3d phase retrieval, eq. (81).

4.1.2 Deteriorating fringes

In the previous section, we saw variations in the normalized absolute difference between separate phase fringes regions. To understand the underlying problem, we distinguish between two groups of phase fringes based on the direction of the side plane surface normal. A reasonable assumption as the yellow, purple and black ROI in fig. 18, each had a surface normal vector either parallel or perpendicular to the tomographic axis. With this distinction, we hope to determine why different regions of phase fringes appear so varied and if there is a correlation between the surface normal direction and the structure of the phase fringe.
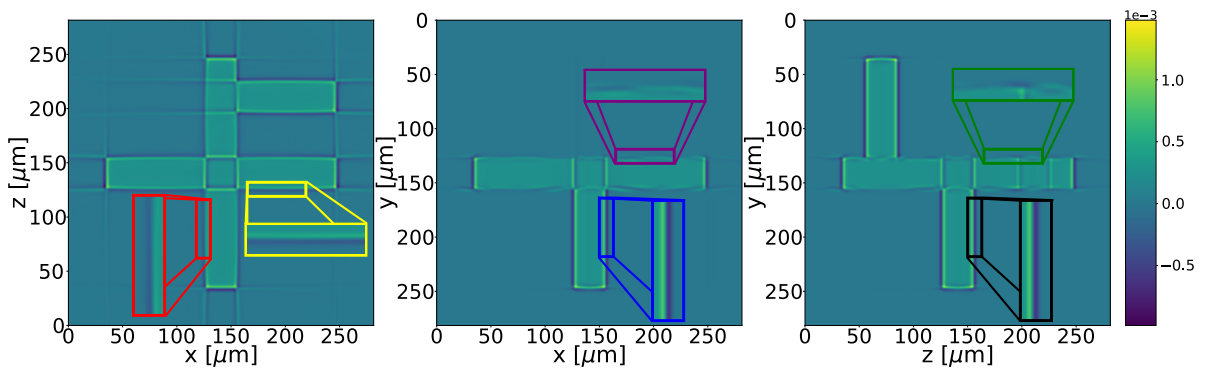

Figure 20: Overview of the reconstructed simulated object with a mass density of 700 kg/m^3. The coloured ROIs indicates a specific edge where the surface normal vector $\vec{n}$ is parallel to a specific axis $\vec{x}, \vec{y}, \vec{z}$. These regions will further be used as the area of interest for additional investigation.

It can qualitatively be seen in fig. 20 that different phase fringe experience a wide range of deformation. This deformation is even more apparent in fig. 21, where the purple phase

fringe exhibits a complete inversion, meanwhile the red region shows slight deviations, and finally black with no visible defects, and being close to idealized phase fringe.
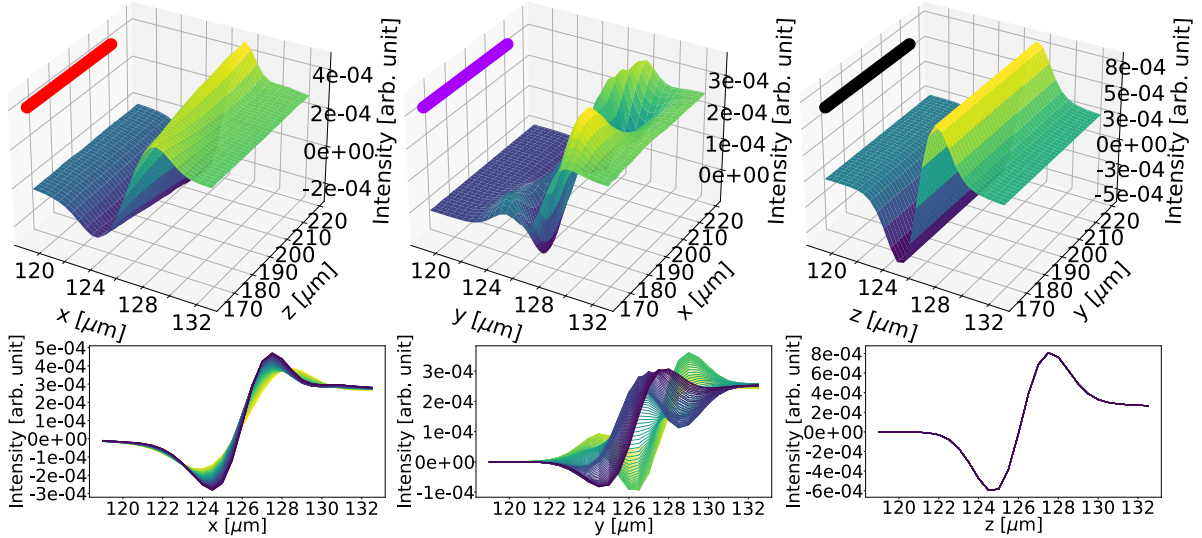

Figure 21: On the upper row the surface plot of three ROIs denoted by (red, purple and black) is shown. These regions are different in that the direction of the surface normal vector $\vec{n}$ is parallel towards $\vec{x}, \vec{y}, \vec{z}$ respectively. Below a transversal view of the fringe can be seen, here the colour map indicates the parallel distance of the edge, with yellow being the closest and purple the farthest.

As such, the first step is to create a way of quantifying how deformed a specific phase fringe is. Given that it is known that all edges in the phantoms are actually straight, we can check the deviation across a fringe, as the perfect edge would have very small deviations. With that reasoning, we start by taking the average across all line-outs along the edge profile $\bar{L}$,

$$\bar{L} = \frac{L_1 + L_2 ... + L_N}{N} \tag{86}$$

where $L_1 + L_2 ... + L_N$ denotes the line-out perpendicular to the edge.

From this point we take the squared deviation of each line from the average $\bar{L}$ and then the square root of the mean to get the standard deviation,

$$\sigma = \sqrt{\left[\frac{1}{N}\sum_{i=1}^{N}(L_i - \bar{L})^2\right]} \tag{87}$$

To make the standard deviation comparable with other fringes, we normalize σ with the maximum value of the intensity for the ROI. The standard deviation can, as such, be represented as a percentage of the maximum value in each specific region, allowing for a relative representation of the standard deviation. In fig. 22 the normalized standard deviation has been plotted against the transverse distance for each of the six regions. Here are two very distinct pairs of fringes, the blue and black, and the rest. This splitting is expected when viewing the features in terms of the sinogram consistency assumption from before, as the blue and black regions will have a smoothly changing integrated thickness.
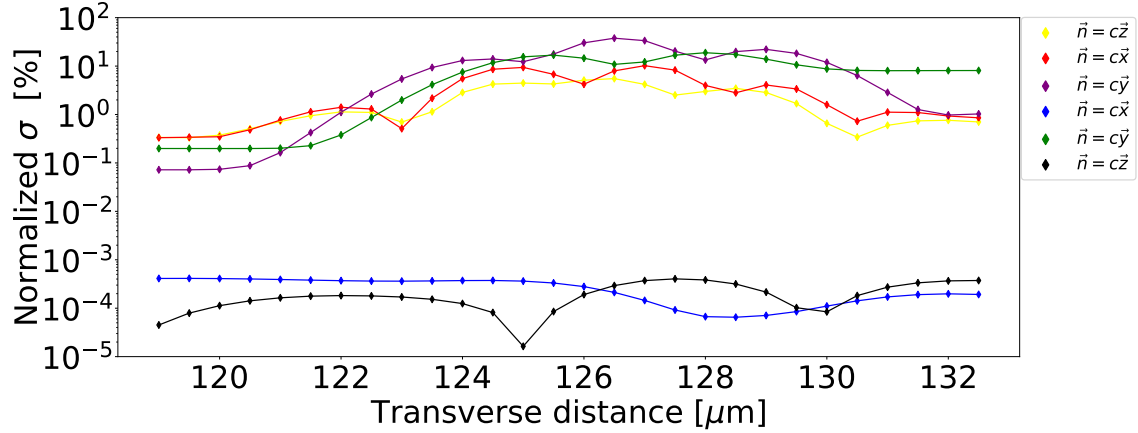
36

Figure 22: The normalized standard deviation for every ROI looking in the transverse direction of the edge.

The yellow and red regions will, by the same reasoning as in section 4.1.1, have a rapidly changing integrated thickness at around 0°, 90° and 180°. For which the reconstruction lacks information, resulting in an unstable phase fringe. In the purple and green regions, the normalized standard deviation is roughly an order of magnitude larger than for the red and yellow ROI, indicating a very deformed fringe. A result which is evident when viewing the transversal view of the purple fringe in fig. 21 as there is a complete inversion of the phase fringe.

To unravel why features perpendicular to the tomographic axis appears distorted, another phantom only consisting of a single rectangular bar is simulated, again utilizing the same simulation parameters. This simulation allows for a better qualitatively comparison of how the Fresnel propagator eq. (15) interacts with the object transmission function eq. (30), as there are no interfering features.
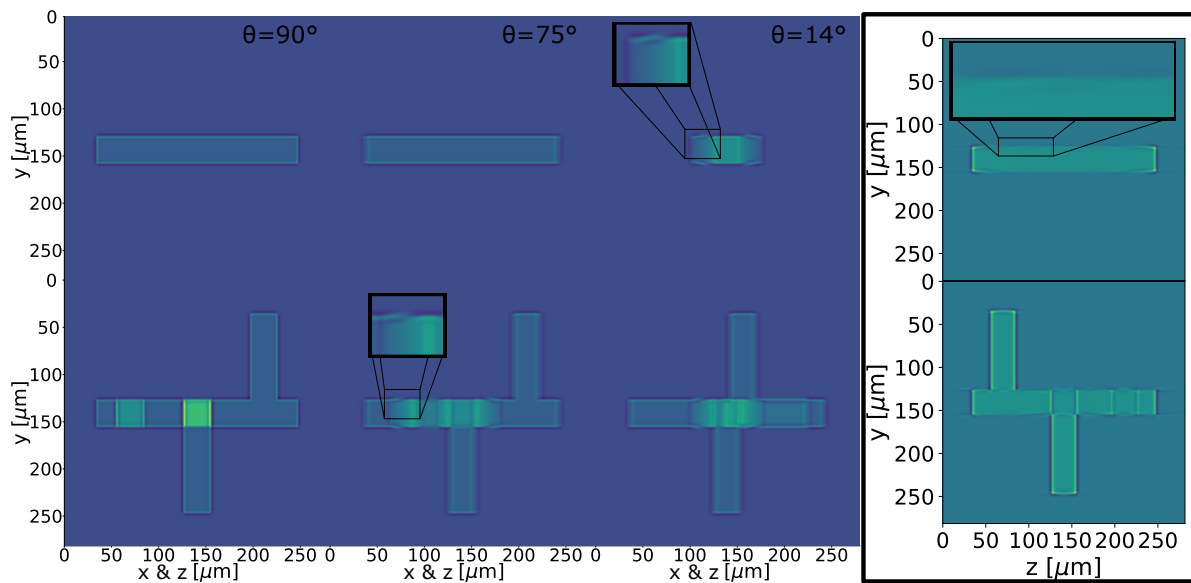

Figure 23: To the left is the retrieve phase contrast image for both phantom with $\theta = [90, 75, 14]°$. To the right is the coronal view of the reconstructed object, here it is evident that the weak phase contrast in the reconstruction is a direct result of the rapidly changing integrated thickness.

In fig. 23 the propagated projections for the pure rectangular cuboid and the original phantom both show a fringe inversion in the angular views where the integrated thickness is large and rapidly changing along $x - z$. Also, the phase fringe in the reconstructed volume for the simplified phantom still exhibits phase contrasts defects. Hence, a fair assumption would be to attribute the inverted phase fringes to the rectangular feature shape, as the integrate thickness between $90°$ and $14°$ is an order of magnitude different, which would result in the observed variant phase fringes. However, to show the exact cause for the fringe inversion, one would ideally need an analytic treatment of the problem.

To continue the analysis from the previous section we again include the effects of mass density on the phase fringe formation, here the same logarithmic scale is used. Thus to see this behaviour we have to simplify the fringe difference even further by taking the average of the normalized standard deviation in each ROI.
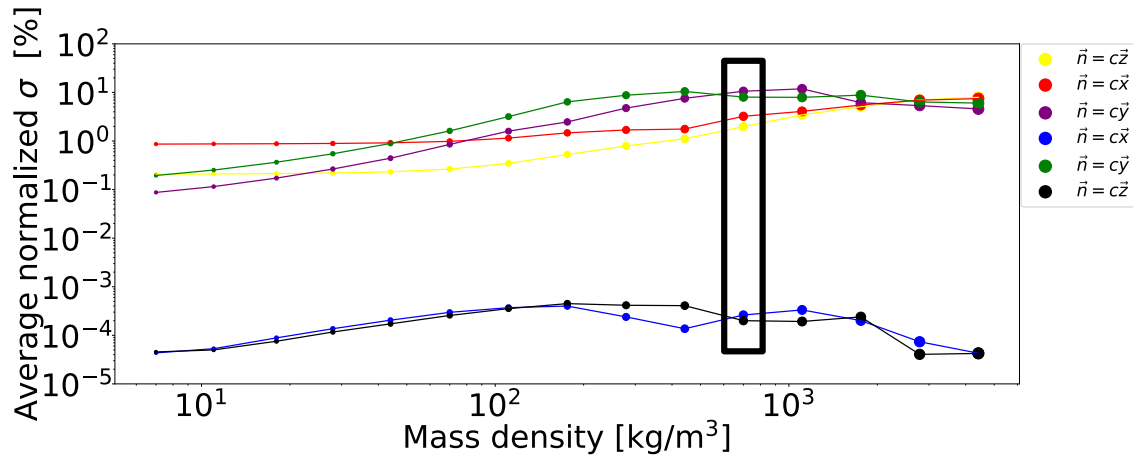

Figure 24: Average normalized standard deviation for each ROI for a logarithmic scale of densities. The black ROI indicates the values for a mass density of 700 kg/m^3.

The resulting figure can be seen in fig. 24 where again each colour represent the specific region of interest. Interesting here is that the green and purple region where the edges surface plane normal vector is aligned to the tomographic axis $\vec{n} = \vec{y}$ appears to start as more stable and grows faster with the increase of the mass density of the object. The blue and black regions have continuously low deviations, regardless of the mass density of the object.

As before, the reason seems to be due to the smooth nature of the sinogram fig. 19, meaning the reconstruction algorithm can correctly reconstruct these features. The same goes for the red and yellow regions, but here the sinogram is not sampled smoothly, for which the reconstruction produces larger defects. Finally, for the green and purple regions, the issue appears to be more involved and is partially the result of phase inversion seen in fig. 23. This phase inversion would, in turn, result in even worse sinogram consistency, further enhancing the already existing defect.

Yet this is only a speculative answer based on qualitative evidence and previously seen effects in the contact regime. To see where these issues are initially coming from, one would need an in-depth analytic treatment of the phase fringe formation. Given that this problem currently can not be solved, the next step is to see how it affects the phase retrieval algorithms.

4.1.3 The effect of phase retrieval on straight edges

The normal approach as stated in section 2.3.1 is to do the phase retrieval for each projection and then reconstruct the object. The advantage of doing it in this order is that we are not required to linearise the in-line contrast function. However as previously outline there are some quite unfavourable effects that occurs for even seemingly simple objects that appears to be a more localized problem. Something that currently can not be account for. Here the analysis is limited to the original simulation with a mass density of 700 kg/m^3 as the effect of the algorithms on a realistic object is of interest.

To apply the phase retrieval a few known parameters are needed, the effective propagation distance, which is given by inverting eq. (44). The effective detector pixel size given by the detector pixel size divided by the magnification, and the energy. Here the effective energy E_{eff} has to be calculated with polychromaticity corrections and is 12.7 keV. The final parameter is the proportionally constant α, which has to be approximated with prior information about the reconstructed object. Due to the simulation, the exact composition is known, and hence the proportionally constant can be calculated.

The following analysis is not aiming to find the optimal filtering parameters but instead is meant to serve as a demonstration of the difference between the 3d and 2d TIE phase retrieval approaches. To that end we use the value of $\alpha = 1300$ given by the polychromatic corrections.
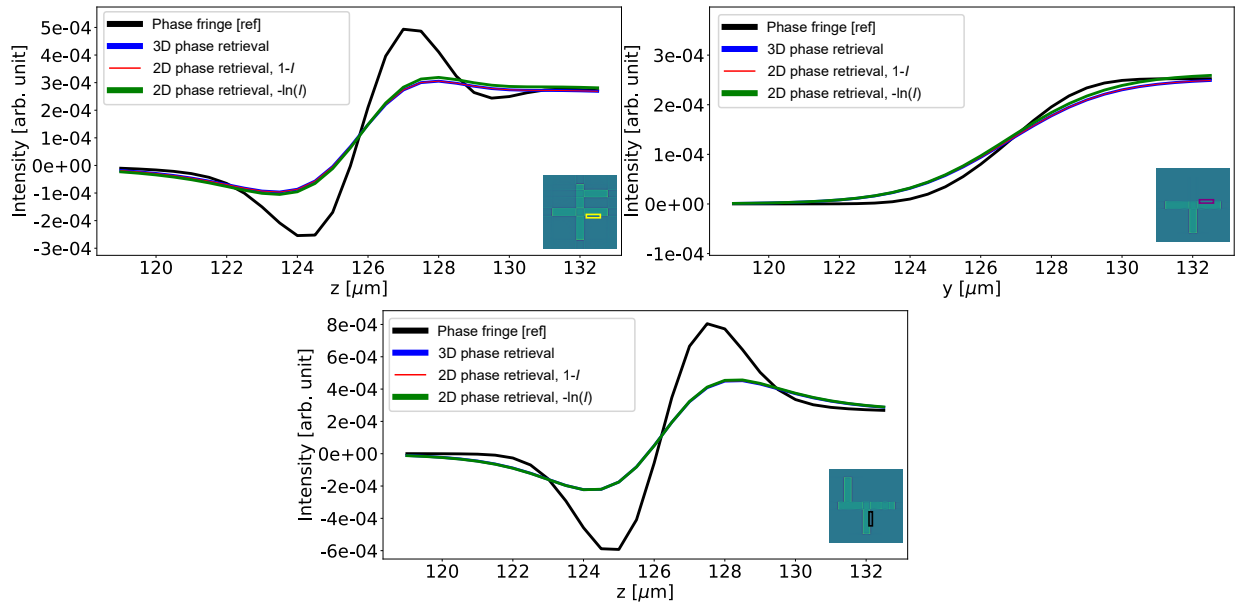

Figure 25: Average phase fringe profiles for three different ROIs. In all plots, the black line represents the non-retrieved phase fringe i.e. the reference. The blue and red line shows the 3d and 2d phase retrieval on an in-line contrast function given as $(1 - I)$. Finally, the green line is the line profile when 2d phase correction has been applied to the $(-\ln(I))$ projections.

We have restricted the analysis to the same regions as in section 4.1.1 given that we showed these regions where roughly equivalent. Additionally, the 2d phase retrieval step for an approximated in-line contrast function is also included to show the direct difference between the two methods.

Even if the in-line contrast function was shown to not be an exact fit, the phase retrieval indicates that the edge location is unaffected, but as before there is a slight intensity difference, only now to a lesser extent. As such the simulations conclude that both methods perform very similarly and there is no significant loss when applying the phase retrieval step after reconstructing the object.
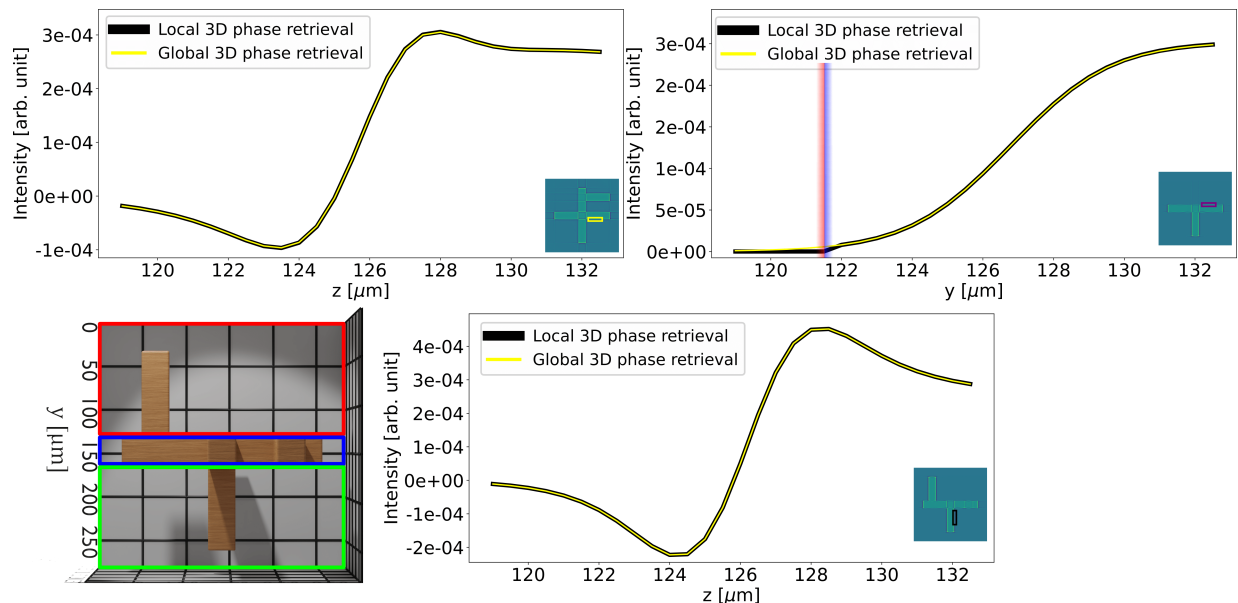

Figure 26: Average line profiles for three different ROIs, black indicates local phase retrieval while the yellow profile is the fringe when retrieval has been applied across the whole object. The local phase retrieval has been applied individually on the three regions going from $y = [0, 121.5]$ μm, $y = [122, 157.5]$ μm and $y = [157.5, 280.5]$ μm denoted by the red, blue and green regions in the bottom left 3d volume. This interface separation is also include in the purple ROI and is indicated by the blue and red gradient line.

Given that the results indicate that the two methods perform very similar, we would now like to know how localized 3d phase retrieval would perform. It would be expected that the filtering is not behaving the same as we are limiting the spatial dimensions and hence restrict the frequency domain, which should result in a difference in the phase filtering. Again, keeping all variables the same the only difference is that we divide the object into three regions in the y direction. These go from $y = [0, 121.5]$ μm, $y = [122, 157.5]$ μm and $y = [157.5, 280.5]$ μm

From fig. 26 we see that local and global phase retrieval effectively retrieves the same object thickness, but issues arise at the interface between regions, as seen in the lineout from the purple ROI in fig. 26. The reason for this is that the local phase retrieval does not contain the outer voxels neighbouring information. To solve this, one would need to deploy a more sophisticated approach to deal with the local region interface than the simple recombination of the local regions used here. This approach could include smoothing at the interface between regions, or the addition of overlapping regions where the interface is constructed from the overlapping values.

However, the results shows that we can restrict the 3d volume to a smaller region and still obtain approximately equal results. A result that is beneficial as a real reconstructed

dataset can be very large. Thus having the option to divide it into a smaller sub-region for analysis is highly useful.

4.2 Wood splinter

4.2.1 Laboratory measurements

Given the result of the varied fringe contrast in the simulations, we tried to reproduce the effect in a real measurement. We choose to measure a wood splinter as it composed of fairly straight cellular structures which should give rise to the effects seen in section 4.1.2. To be able to see the dependence on the edge orientation the splinter was measured in two different sample orientations. In this way each different category of edges would be flipped and compared, according to the results from the simulations.
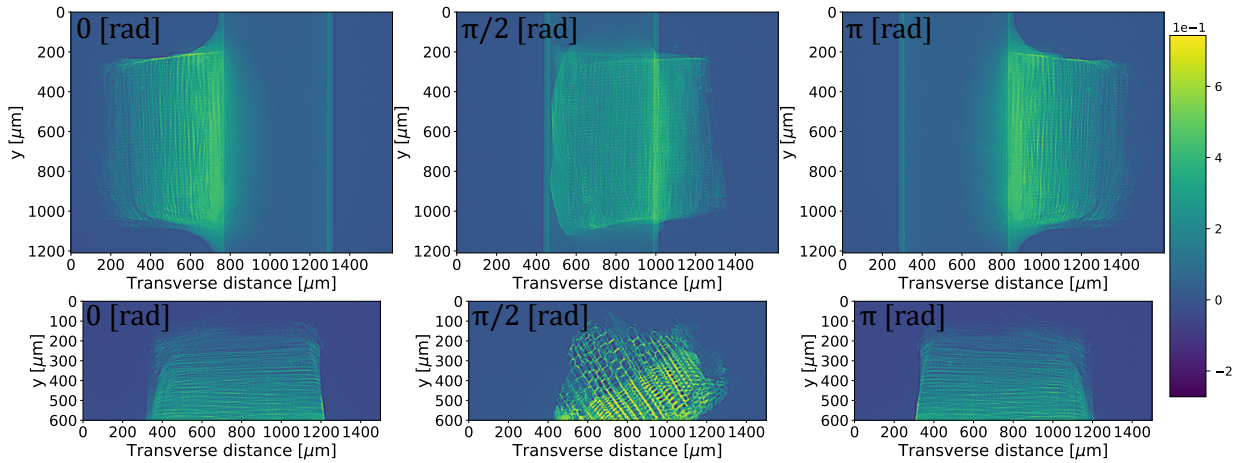

Figure 27: The projections of the vertically (upper), and horizontally (lower) aligned sample. The images from left to right show the projection of 0, 90°, 180° respectively.

The normal experimental alignment, section 3.3, was done and the sample was prepared by gluing the splinter with epoxy onto a small Kapton tube. To ensure stability, the system was allowed to rest for several hours before starting the measurement and each orientation was measured more than once. When the dataset for the first orientation had been collected the second one was retrieved by flipping the kapton tube on its side such that only the splinter was inside the FoV, see fig. 27. Additionally the distance where set to be the same as in the simulations. Therefore the total distance (z_{tot}) was set to 9.9 cm, with the sample to detector distance z_2 being 0.9 cm, giving a magnification of $M = 1.1$.

Once datasets from both orientations were collected, the data was pre-processed as outline in section 3.4 and reconstructed using parallel beam geometry. Unfortunately, even the best dataset for each orientation resulted in reconstructions with noticeable artefacts, as can be seen in fig. 28. Thus, it was difficult to determine if the cause for the impaired quality was due to the sample orientation or other factors. The artefacts appear to be the result of a misalignment pitch angle ν as the reconstruction has clear stripes along the tomographic axis y, which is accompanied with this type of misalignment section 3.1.3. Thus the defect

41

cannot easily be solved by known pre-processing algorithms and will subsequently impair the analysis.
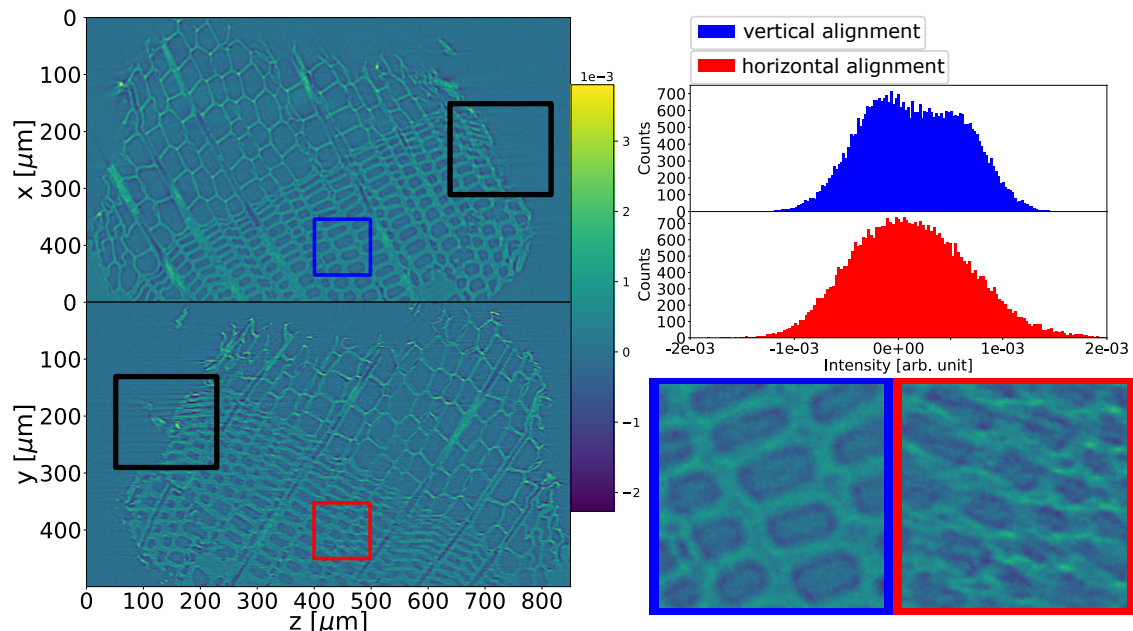

Figure 28: View of a smaller part of the reconstruction for the two different sample orientations. The upper slice shows the reconstruction for vertical alignment to the tomographic axis, while the lower one is horizontally aligned. The black ROI indicates a region where the horizontal dataset shows stripe artefacts parallel to the tomographic axis. The blue and red ROI displays a region with similar features. These two regions have their intensity represented as a histogram in the upper right corner.

Therefore, instead of quantitatively comparing the same features throughout the volume, we will have to limit ourselves to a qualitative analysis of potential defects. In fig. 28 and fig. 29 we can see stripe artefacts parallel to the tomographic axis, which appear similar to the defects we saw in the simulations. Yet as the artefact is only present for a few of the feature it makes it less likely that the effect is related to the sample orientation.

Another general defect given from the blue and red regions in fig. 28 and fig. 29 is that the horizontally sampled reconstruction shows a lowered contrast. Something that could be attributed to the fact that the object is not perfectly symmetric and is longer on one side. This is further evident when looking at the 90° projection in fig. 27. Here the absorption is much higher, which would result in it and the neighbouring angular region containing lacking sinogram consistency, resulting in a reconstruction with less contrast.

If we assume that the misalignment errors are stationary for both measurements, a fair assumption as the misalignment drift should be small. Then the decreased contrast could be evidence of the same effect from the simulations. However, it has to be stated that due to the splinter being rectangular the effect is exacerbated for the horizontal alignment, and the decreased contrast would be present for unaligned features as well. The reason for this comes directly from Beer-Lambert law, eq. (34), as the thickness z is higher in horizontal alignment. Thus to obtain better evidence for fringe defects due to the alignment features, one would ideally have a cubic sample, as it would alleviate the decreased contrast coming

from the shape. To that end, the cause for the lowered fringes contrast remains indecisive, as there are two potential candidates that both explain the decreased contrast.
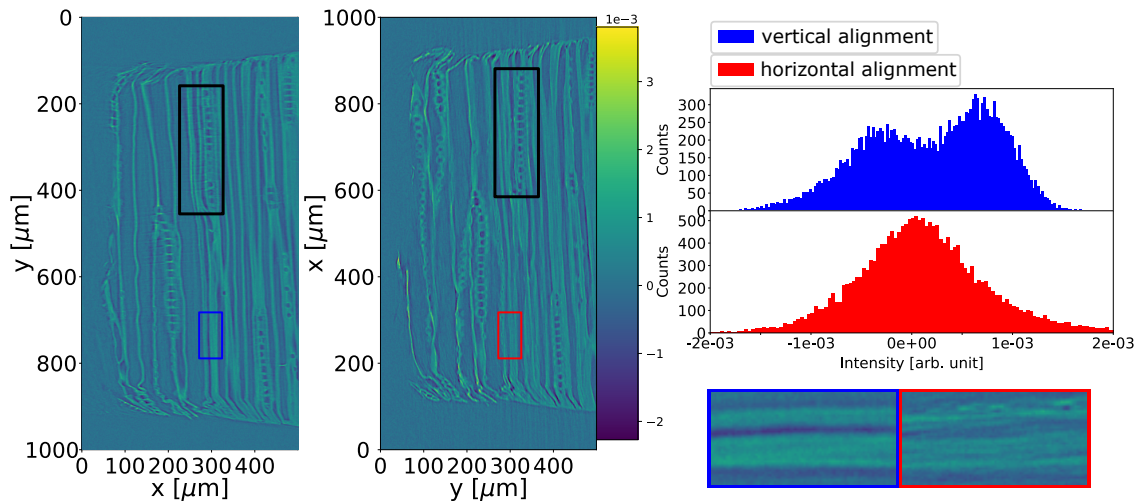

Figure 29: Another smaller region of the reconstructions. Here the left image is vertically aligned, while the right one is horizontally aligned. The black ROI indicates a region in the vertical measurement where the stripe artefacts parallel to the tomographic axis occurs. The blue and red ROI again shows an area where both datasets have a similar feature, and to the left is the histograms for these regions.

The main objective of this work is to compare how the two TIE phase retrieval methods behave. But as the horizontal measurement exhibits poor contrast, the analysis will be restricted to the blue region of the vertically aligned measurement, seen in fig. 29. Here we follow the same methodology as in section 4.1.3, meaning that the in-line contrast function has been approximated for the use of 3D phase retrieval and kept as $-\ln(I)$ for the standard 2d retrieval.
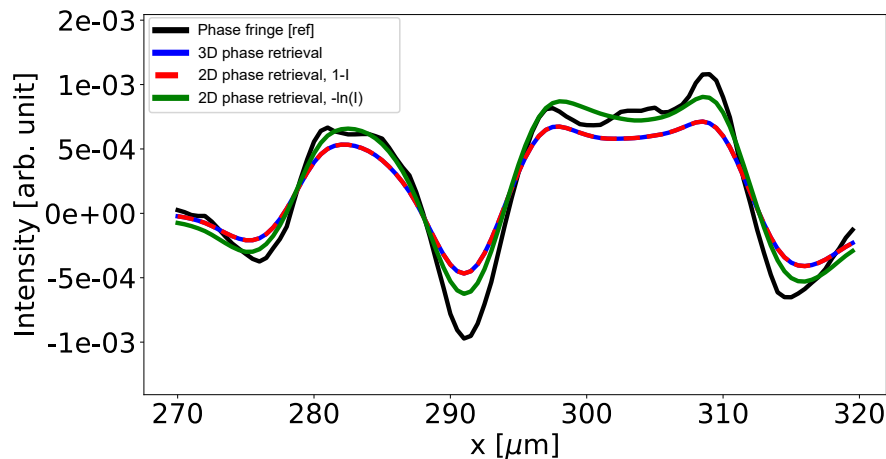

Figure 30: Average phase fringe profiles for the blue ROI in fig. 29. The black line shows the line profile for the phase fringe i.e. the reference, note that the in-line contrast still is approximated as $(1 - I)$ due to the finds in section 4.1.1. The blue and red dashed line shows the 3d and 2d phase retrieval on $(1 - I)$, which are still approximately giving the same results. Finally, the green line is the line profile when 2d phase correction has been applied to the $(-\ln(I))$ projections.

43

We have also opted to include the 2d phase retrieval on an in-line contrast function given by $(1 - I)$ to see if there are any direct difference between the two. Additionally, the final result from section 4.1.3 is used to restrict the 3D phase retrieval to half of the object, this as only half of the reconstructed volume contains the wood splinter.

The discrepancy between the 2d and 3d phase retrieval approaches is higher than what the previous simulation have shown, fig. 30. This discrepancy is due to the larger object, as the absorption is an order of magnitude larger than in the simulations. As a result, the laboratory measurement has a lesser agreement of eq. (74) giving weaker contrast when applied. Even with decreased contrast due to an approximated in-line contrast function, the edge profile remains largely intact, as can be concluded by the location of the maxima.

With this information in mind, 3d phase retrieval has a case of being the option for performing phase corrections in localized regions for multi-material structures. As the phase retrieval parameters can be locally tuned, to still hold the mono-material approximation. Something that the 2d method severely struggles with, due to the integrated object information of the projections. Hence there might be more to gain with optimal phase retrieval parameter than is lost by the decreased contrast. However, the 2d phase retrieval would be superior for homogeneous samples where one step phase retrieval suffice as the contrast is higher.

Furthermore, for the 3d case, it could be imagined that the phase retrieval algorithm and a segmentation algorithm is combined. Here the segmentation algorithm would try to distinguishing different features based on a set of constraints. Thus, the segmentation could deal with the categorization of distinct phase regions. These local phase fringes could then be fitted with a phase-contrast function to receive the proportionally constant. Alternatively, an iterative method could be deployed where each region is phase retrieved until a specific criterion is reached. In this way, the combined approach would be constrained based on physical parameters, which would limit the ordinary subjective selection of parameters.
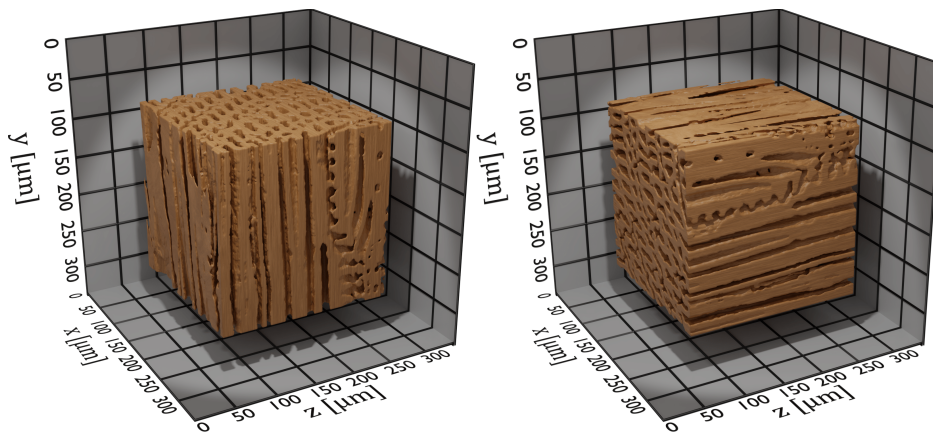
4.2.2 Segmentation as phantom

Figure 31: Illustrative overview of the two different orientation for the segmented wood splinter.

In section 4.1 the phantom was created to give ill-behaved features, and as the measurement only gave hints to the existence of the defects due to the sample orientation another simu-

lation will be performed. This simulation will use a segmented version of an earlier wood splinter measurement with better quality. The motivation for this simulation is that it could serve as a bridge between the simplified phantom simulations and the real experiment.

To limit other potential defects only a symmetric cube of the segmentation will be used, as we would otherwise run into the same problem as in the laboratory measurement when the tomographic axis is changed. The simulation also assumes the distances from before, that being a total distance (z_{tot}) of 9.9 cm, with the sample to detector distance z_2 being 0.9 cm. Due to the larger matrix size, we also increased the number of projections to 501.
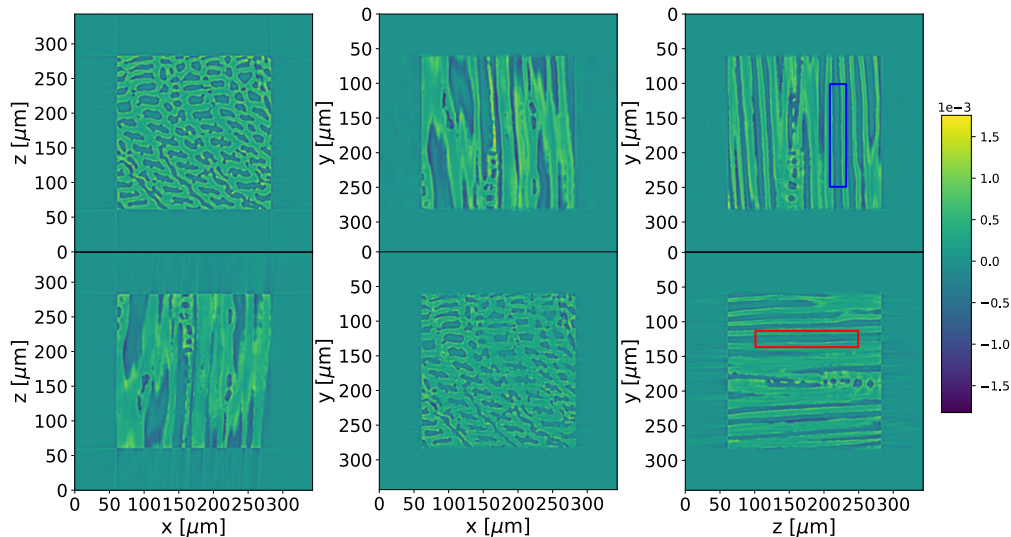

Figure 32: Reconstruction of wood splinter oriented in two different directions. The upper row of slices are when the object has be rotated parallel with the length of the features. For the lower row the object the opposite is true, and the object features are now perpendicular to the tomographic axis. The blue and red ROI indicates the regions we will give a closer view.

From the reconstruction of the two different orientations, fig. 32, it can qualitatively be seen that when feature are vertically aligned along the tomographic axis, i.e. the edge surface normal vector is perpendicular to the tomographic axis we get a higher contrast. A better view can be seen in fig. 33 where the average fringe profile and histograms for the blue and red regions are depicted.

It can be seen that there is an overall decrease of contrast for the horizontally aligned sample. Yet, more interesting is that the phase profile has changed quite drastically, with both edges being shifted inwards by a few microns. Given that the sample might contain both of these aligned features in a given measurement there will be a definite possibility for higher uncertainties in the size of features for the feature which are horizontally aligned.

In simulations, the edge shift effect can be quantified as the ground truth is known, given the phantom. However, for laboratory measurements, the ground truth is unknown, and real samples are generally larger. Meaning that the edge shift might be even more substantial for laboratory measurements, resulting in larger features size uncertainties. Thus to quantify the edge shift, a sample with a well-defined size would be needed, in addition to the other previously mentioned requirement of a cubic structure and better alignment procedures, section 4.2.1.

Even if we have shown the validity of 3d phase retrieval in the prior sections, the result of how these artefacts propagate in the phase retrieval is of value. fig. 34 shows the phase profile for both sample orientation, with the ground truth edge indicated by the gradient vertical line.
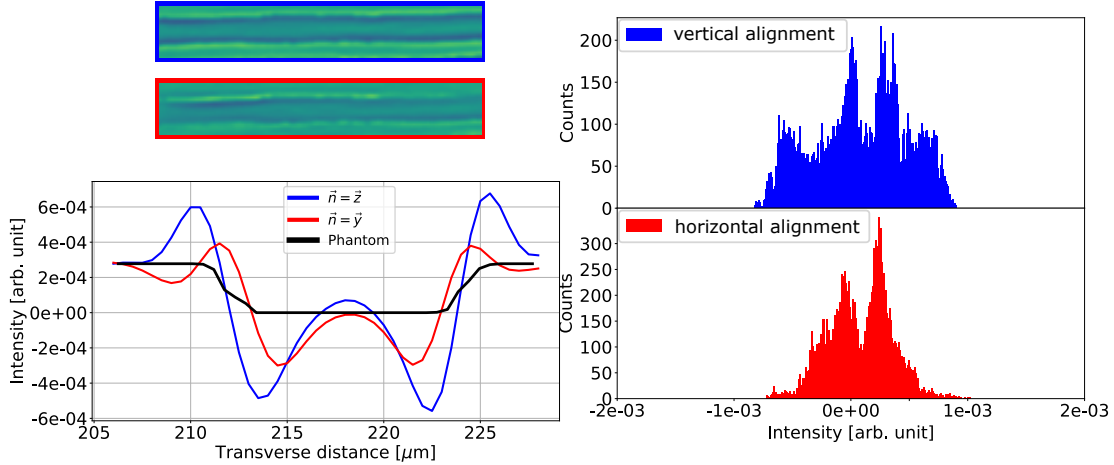

Figure 33: To the left is the average phase fringe profiles for the blue and black ROI in fig. 32. The blue line depicts the phase fringe when the objects edge surface normal is perpendicular to the tomographic axis. The red line shows the same area, but for an object with a surface normal parallel to the tomographic axis, and the black line is the average phantom edge profile indicating the true edge. The right plots show the histograms of both regions, with the colour representing the same areas as before.

For these simulations, both phase retrieval methods perform well, but the edge shift is still present in the horizontal measurement where the edge surface normal is parallel to the tomographic axis. This result is natural given that the initial phase fringe already indicated the edge shift. As such, the features size uncertainties are still present after phase retrieval, meaning that the size information is effectively lost when the sample has features aligned with the optical axis.
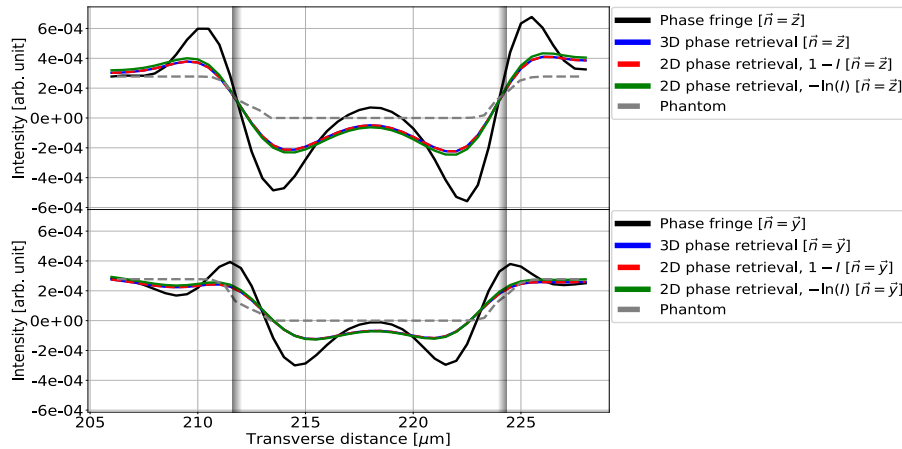

Figure 34: Line profiles for the phase retrieved simulated wood splinter. The upper plot shows the phase fringe for $\vec{n} = \vec{z}$ and its subsequent profiles after phase retrieval. The same is true for the lower one, only here the surface normal is parallel to the tomographic axis. The grey dashed line now depicts the phantom profile and the two gradient vertical lines indicate the phantom edges.

46

5 Conclusions

In this work, we have demonstrated, via numerical modelling, the validity of approximating the in-line contrast function by a first-order Taylor expansion in PB-PCT for rectangular-shaped objects, section 4.1.1. However, the object shape gave rise to unique phase-contrast effects for edges oriented perpendicular to the tomographic axis and for features that experience rapidly changing integrated thickness while rotated. These effects both lead to increased phase contrast, which we argue as partially interlinked in that both decreased sinogram consistency constraints, resulting in a faulty reconstruction, section 4.1.2. The 2d and 3d phase retrieval method based on the TIE framework has also been tested, showing comparable results. The 3d algorithm has further been limited to local regions for phase retrieval, where it performed equivalent to the global approach except for values close to the interface between local regions, section 4.1.3.

The simulations produced different phase contrast on features oriented perpendicular and parallel to the tomographic axis. For this reason, two sets of laboratory measurement on a wood splinter were acquired. These measurements had the sample oriented vertically and then horizontally, allowing the effects of aligned features to be investigated. Here a decreased contrast was observed when the internal features were perpendicular to the tomographic axis. We could not exclusive attribute this reduced contrast to the alignment, as there was an inherent increased absorption due to the rectangular shape of the sample. Resulting in indecisive evidence as two potential candidates both explained the seen effects, section 4.2.1.

Additionally to the reduced contrast in the horizontally aligned measurement, there were misalignment issues with the pitch angle, limiting the quantitative analysis. Hence the phase retrieval comparison was restricted to the measurement with the sample vertically aligned as it had better feature contrast. In this comparison, the methods showed similar results in the retrieved feature size. But due to the large object size of the wood splinter, the in-line contrast function approximation was in less agreement, leading to decreased contrast for the 3d algorithm compared to the 2d approach. As such, the 2d phase retrieval was deemed to be superior for homogeneous samples where one step phase retrieval suffice. Meanwhile, the 3d method could see a use for samples where local phase retrieval outweighs the decreased contrast.

Moreover, the local phase retrieval provided by the 3d approach could potentially be combined with segmentation. In this way, the segmentation could deal with the categorization of different phase regions, where the local phase fringes can be fitted with a phase-contrast function to receive the corrected phase retrieval parameters, limiting the need for prior material knowledge. Alternatively, an iterative method could be deployed where each region is phase retrieved until a specific criterion is reached.

In hopes of bridging simulations and experiments, the effect of internally aligned features was also tested in simulations where the phantom had been created from a segmentation of a previous wood splinter measurement with higher quality, section 4.2.2. These simulations showed related artefacts seen in the laboratory measurement in terms of reduced contrast, providing further evidence to the hypothesis that the decreased contrast is associated with the feature alignment. It also revealed that when features are perpendicular to the tomographic axis, the phase-contrast is shifted from the true edge. Indicating that features size uncertainties are present whenever features are aligned with the optical axis.

6   Acknowledgements

This thesis would not have been achievable without the assistance from my supervisors Hanna Dierks and Jesper Wallentin. I would therefore like to extend my gratitude towards both for all the support through the year and for allowing me to be a part of the tomography group. A special thanks to Hanna for taking me under her wing and teaching me about X-ray physics and the intricacies of the lab-work for propagation-based X-ray phase-contrast tomography. I would also like to thank Pablo Villanueva Perez for introducing me to Jesper Wallentin's group.

References

[1] M. Herbig, A. King, P. Reischig, H. Proudhon, E. M. Lauridsen, J. Marrow, J. Buffière, and W. Ludwig. 3-D growth of a short fatigue crack within a polycrystalline microstructure studied using combined diffraction and phase-contrast X-ray tomography. *Acta Materialia*, 59(2):590–601, 2011.

[2] P. Baran, S. Pacilè, Y. I. Nesterets, S. C. Mayo, C. Dullin, D. Dreossi, F. Arfelli, D. Thompson, D. Lockie, M. McCormack, et al. Optimization of propagation-based x-ray phase-contrast tomography for breast cancer imaging. *Physics in Medicine & Biology*, 62(6):2315, 2017.

[3] M. Krenkel, C. Töpperwien, M.and Dullin, F. Alves, and T. Salditt. Propagation-based phase-contrast tomography for high-resolution lung imaging with laboratory sources. *AIP Advances*, 6(3):035007, 2016.

[4] D. Paganin, S. C. Mayo, T. E. Gureyev, P. R. Miller, and S. W. Wilkins. Simultaneous phase and amplitude extraction from a single defocused image of a homogeneous object. *Journal of microscopy*, 206(1):33–40, 2002.

[5] D. A. Thompson, Y. I. Nesterets, K. M. Pavlov, and T. E. Gureyev. Fast three-dimensional phase retrieval in propagation-based X-ray tomography. *Journal of synchrotron radiation*, 26(3):825–838, 2019.

[6] P. M. Joseph and R. D. Spital. The exponential edge-gradient effect in x-ray computed tomography. *Physics in Medicine & Biology*, 26(3):473, 1981.

[7] D. Paganin. *Coherent X-ray optics*. Oxford University Press on Demand, 2006.

[8] A. Ruhlandt. *Time-resolved X-ray phase-contrast tomography*. Universitätsverlag Göttingen, 2018.

[9] Y. I. Nesterets, S. W. Wilkins, T. E. Gureyev, A. Pogany, and A. W. Stevenson. On the optimization of experimental parameters for x-ray in-line phase-contrast imaging. *Review of scientific instruments*, 76(9):093706, 2005.

[10] J. Als-Nielsen and D. McMorrow. *Elements of modern X-ray physics*. John Wiley & Sons, 2011.

[11] U. Lundström. *Phase-contrast x-ray carbon dioxide angiography*. PhD thesis, KTH Royal Institute of Technology, 2014.

[12] H. Dierks and J. Wallentin. Experimental optimization of X-ray propagation-based phase contrast imaging geometry. *Optics Express*, 28(20):29562–29575, 2020.

[13] M. Töpperwien. *3d virtual histology of neuronal tissue by propagation-based X-ray phase-contrast tomography*, volume 25. Universitätsverlag Göttingen, 2018.

[14] T. Buzug. *Computed Tomography: From Photon Statistics to Modern Cone-Beam CT, Two-Dimensional Fourier-Based Reconstruction Methods*. Springer, 2008.

[15] A. C. Kak and M. Slaney. Principles of Computerized Tomographic Imaging, Algorithms for Reconstruction with Nondiffracting Sources. *Classics In Applied Mathematics. Philadelphia, PA, USA: Society for Industrial and Applied Mathematics*, 2001.

[16] D. Gürsoy, Y. P. Hong, K. He, K. Hujsak, S. Yoo, S. Chen, Y. Li, M. Ge, L. M. Miller, Y. S. Chu, et al. Rapid alignment of nanotomography data using joint iterative reconstruction and reprojection. *Scientific reports*, 7(1):1–12, 2017.

[17] R. Schulze, U. Heil, D. Groβ, D. D. Bruellmann, E. Dranischnikow, U. Schwanecke, and E. Schoemer. Artefacts in CBCT: a review. *Dentomaxillofacial Radiology*, 40(5):265–273, 2011.

[18] T. Stankevič, C. Engblom, F. Langlois, F. Alves, A. Lestrade, N. Jobert, G. Cauchon, U. Vogt, and S. Kubsky. Interferometric characterization of rotation stages for X-ray nanotomography. *Review of Scientific Instruments*, 88(5):053703, 2017.

[19] N. T. Vo, R. C. Atwood, and M. Drakopoulos. Superior techniques for eliminating ring artifacts in X-ray micro-tomography. *Optics express*, 26(22):28396–28412, 2018.

[20] D. Kazantsev, V. Pickalov, S. Nagella, E. Pasca, and P. J. Withers. TomoPhantom, a software package to generate 2D–4D analytical phantoms for CT image reconstruction algorithm benchmarks. *SoftwareX*, 7:150–155, 2018.

[21] G. N. Inari, M. Pétrissans, A. Pétrissans, and P. Gérardin. Elemental composition of wood as a potential marker to evaluate heat treatment intensity. *Polymer degradation and stability*, 94(3):365–368, 2009.